





Cite this: *Phys. Chem. Chem. Phys.*,
2022, 24, 7144

Interactions of $\text{Si}^+(\text{}^2P_J)$ and $\text{Ge}^+(\text{}^2P_J)$ with rare gas atoms (He–Rn): interaction potentials, spectroscopy, and ion transport coefficients†

Alexander R. Davies,^a Aiden Cranney,^a Larry A. Viehland ^{*b} and
Timothy G. Wright ^{*a}

Accurate interatomic potentials were calculated for the interaction of a singly-charged silicon cation, Si^+ , with a single rare gas atom, RG (RG = Kr–Rn), as well as a singly-charged germanium cation, Ge^+ , with a single rare gas atom, RG (RG = He–Rn). The RCCSD(T) method and basis sets of quadruple- ζ and quintuple- ζ quality were employed; each interaction energy is counterpoise corrected and extrapolated to the basis set limit. The lowest electronic term ($\text{}^2P$) of each cation was considered, and the interatomic potentials calculated for the diatomic terms that arise from these: $\text{}^2\Pi$ and $\text{}^2\Sigma^+$. Additionally, the interatomic potentials for the respective spin–orbit levels were calculated, and the effect on the spectroscopic parameters was examined. Variations in several spectroscopic parameters with the increasing atomic number of RG were examined. The presence of incipient chemical interaction was also examined via Birge–Sponer-like plots and various population analyses across the series. In the cases of heavier RG, these were consistent with a small amount of electron transfer from the heavier RG atom to the cation, rationalizing the spin–orbit splittings. This was also supported by the observed larger-than-expected spin–orbit splittings for the Si^+ –RG complexes. Finally, each set of RCCSD(T) potentials including spin–orbit coupling was employed to calculate transport coefficients for the cation moving through a bath of the RG. The calculated ion mobilities showed significant differences for the two atomic spin–orbit states, arising from subtle changes in the interaction potentials.

Received 14th December 2021,
Accepted 25th February 2022

DOI: 10.1039/d1cp05710c

rsc.li/pccp

1. Introduction

Silicon and germanium have wide-ranging applications in electronic components, and the fabrication of these often involves the need to produce thin layers, such as by laser ablation or plasma-enhanced chemical vapour deposition (CVD).^{1–4} In such systems, Si^+ or Ge^+ (as well as many other) ions may be expected to be present, although these are not always explicitly considered. Attempts to model and refine the chemical processes depend on being able to determine reaction kinetics and model the chemistry comprehensively and reliably – such modelling and kinetic studies with atmospheric ligands has been carried out by Plane and co-workers for silicon⁵ and also several metal ions.^{6–12}

Silicon atoms are present in the Earth's upper atmosphere as a result of the ablation of meteoroids.¹³ Rapid reaction of

Si with O_2 or O_3 leads to the formation of SiO , and then SiO^+ by subsequent charge transfer; the reaction between SiO^+ and O then leads to the production of Si^+ ions in the upper atmosphere.⁵ This leads to Si^+ having an abundance similar to those of Fe^+ and Mg^+ above 100 km, although very little is found below 95 km,⁵ which has attracted significant interest.^{1,5,14} Silicon ions are also present in both the solar wind¹⁵ and dense interstellar clouds, where ion–molecule reactions between Si^+ and H_2O are thought to be key in forming SiO^+ a key silicon-containing species.¹⁷ Silicon ion chemistry is also important in other applications,¹⁸ such as flames¹⁹ and in state-of-the-art electronics fabrication.²⁰

Germanium is known to be present in meteorites,²¹ and Ge^+ has also been detected in the interstellar medium (ISM).²² Rationalizing concentrations observed in the latter depends on understanding the process of depletion, whereby gas phase ions are trapped within dust particles.²³ Efforts to study this phenomenon are ongoing, but understanding is hampered by the uncertainty of the requisite data.²⁴ Additionally, although apparently not considered in the literature, cooling of both Si^+ and Ge^+ ions in astrochemistry, *via* interaction/complexation with prevalent He, may be possible – in the same way as has

^a School of Chemistry, University Park, University of Nottingham,
Nottingham NG7 2RD, UK. E-mail: tim.wright@nottingham.ac.uk

^b Science Department, Chatham University, Pittsburgh, Pennsylvania 15232, USA.
E-mail: viehland@Chatham.edu

† Electronic supplementary information (ESI) available. See DOI: 10.1039/d1cp05710c



been discussed with C^+ ions.^{25,26} Also, for RG = rare gas, both Ge^+-RG and $Ge^{2+}-RG$ (RG = Ne–Xe) have been detected in mass spectrometric experiments,²⁷ indicating that these are relatively stable species; however, no spectroscopic studies of these species exists, to the authors' knowledge.

Obtaining detailed kinetic information for modelling atmospheric or interstellar chemistry often involves flow tube experiments, with such having been carried out for Si^+ .^{28–30} In these experiments, obtaining accurate ion mobility data for Si^+ in RG is important for determining non-chemical loss mechanisms, as the flow gases are usually rare gases, and the Ge^+ results herein will be of use in corresponding kinetics studies. Mobilities also determine the relative energy of ions in flow and drift tubes,³¹ and so there are wider incentives for obtaining such data.³²

Molecular complexes are often described as being “pre-reactive” species and can be used to interrogate nascent interactions that occur prior to full chemical reaction. The interactions of atomic cations with rare gas atoms are amongst the simplest interactions that can be investigated, and although even the lightest RG atoms have been hypothesised to exhibit chemical interactions (see, for example ref. 33 and 34), in the present work these evolve from physical interactions, with the weakly-polarizable He atom, with possibility of chemical interactions only occurring for the more-polarizable Kr, Xe and Rn atoms.

The initial stage in investigating such interactions is through the determination of the interatomic potentials. These can then be used to determine values of various spectroscopic parameters, and the trends in these can reveal the changing nature of the interaction, for example as the atomic number of the RG atom increases. Additionally, the electronic wavefunctions can be analysed to obtain populations, and to determine whether electrons remain localized on a moiety or are shared between the interacting species. Although delocalization of electron density from one nuclear centre is an obvious indicator of chemical interaction, hybridization can also be considered as a chemical effect.³⁵ Reliable interaction potentials can also be employed in the calculation of a range of quantities including collision cross sections – important in the calculation of ion transport data and atomic collisional energy transfer.

In the present paper, we extend our earlier work on the C^+-RG (RG = He–Xe)^{36,37} and Si^+-RG (RG = He–Ar)³⁸ complexes. We consider Si^+ interacting with the heavier RG atoms (RG = Kr–Rn) and Ge^+ interacting with RG = He–Rn. In each case, we shall investigate the interatomic potentials that arise from the lowest atomic asymptotes of the open-shell M^+-RG complex, $M^+(^2P_J) + RG(^1S_0)$, $J = \frac{1}{2}$ and $\frac{3}{2}$, $M = Si$ or Ge . The asymptotes arise from the closed-shell ground state configuration of the RG atom, and the lowest energy electronic configuration for the M^+ : $[Ne]3s^23p^1$ and $[Ar]3d^{10}4s^24p^1$, for $M = Si$ and Ge , respectively, once the spin-orbit interaction is included. From these interatomic potentials, we shall obtain accurate spectroscopic constants and investigate whether the spin-orbit interaction affects these significantly. For each of the two spin-orbit states arising from the ground electronic states of the atomic cations,

the spin-orbit potentials are also used to obtain transport coefficients for the cation moving through a bath of RG.

When a closed-shell RG atom interacts with a cation, degenerate atomic states may become split. In the present cases, initially in the absence of the spin-orbit interaction, the 2P ground electronic term of M^+ gives rise to a lower-energy $^2\Pi$ and a higher-energy $^2\Sigma^+$ diatomic term. However, it is, of course, the spin-orbit levels that are present experimentally. Upon the inclusion of the spin-orbit interaction, the $M^+(^2P)$ term splits into a lower $^2P_{1/2}$ and a higher $^2P_{3/2}$ level, with separations of 287.24 cm^{-1} and 1767.36 cm^{-1} , for $M = Si$ and Ge , respectively.³⁹ The spin-orbit interaction causes the $^2\Pi$ diatomic term to split into $^2\Pi_{1/2}$ and $^2\Pi_{3/2}$ levels, and the $^2\Sigma^+$ term becomes $^2\Sigma_{1/2}^+$; the lowest $^2\Pi_{1/2}$ level correlates to the $M^+(^2P_{1/2}) + RG(^1S_0)$ asymptote, while the $^2\Pi_{3/2}$ and $^2\Sigma_{1/2}^+$ levels both correlate to $M^+(^2P_{3/2}) + RG(^1S_0)$.

Since Ω levels of the same value can mix, an interaction between the $^2\Pi_{1/2}$ and $^2\Sigma_{1/2}^+$ levels is expected. At most internuclear separations, the mixing of these is expected to be small, and so we consider the resulting $\Omega = 1/2$ levels as perturbed versions of the original $^2\Pi_{1/2}$ and $^2\Sigma_{1/2}^+$ levels, and maintain these Russell–Saunders labels. In principle, additional, smaller mixings occur, involving higher energy atomic states, but these are not considered here.

To our knowledge there has been no published work, experimental or theoretical, on Si^+-RG (RG = Kr–Rn), or Ge^+-RG (RG = He–Rn), but we shall comment on some published spectroscopic results for Si–Ar and Ge–Ar.

2. Computational methodology

2.1 Quantum chemistry

Interaction potentials with and without the spin-orbit interaction have been computed for the diatomic states arising from the lowest atomic asymptotes of M^+-RG in the following manner. Energies over a wide range of internuclear separations within the range $0.8\text{--}100\text{ \AA}$ were evaluated at the RCCSD(T) level of theory as implemented in MOLPRO.^{40,41} Standard basis sets were employed: aug-cc-pVXZ for He;⁴² aug-cc-pwCVXZ⁴³ basis sets ($X = Q, 5$) for Ne, Si and Ar; while for Ge, Kr, Xe, and Rn, small-core relativistic effective core potentials (ECPs) were employed to describe the innermost electrons (ECP10MDF for Ge and Kr, ECP28MDF for Xe and ECP60MDF for Rn) together with the standard aug-cc-pwCVXZ-PP valence basis sets^{44,45} to describe the non-ECP electrons. In the RCCSD(T) treatment, the following orbitals were frozen for Si^+-RG : Si ($1s2s2p$); Kr ($3s3p3d$); Xe ($4s4p4d$); and Rn ($5s5p5d$). For the RCCSD(T) calculations on Ge^+-RG , the following orbitals were frozen: Ge ($3s3p$); Ne ($1s$); Ar ($1s2s2p$); Kr ($3s3p$); Xe ($4s4p$); and Rn ($5s5p$). Interaction energies at each separation were counterpoise (CP) corrected to account for basis set superposition error. To include the spin-orbit interaction, the CP-corrected RCCSD(T) interaction energies were used as the unperturbed eigenvalues of the Breit-Pauli spin-orbit matrix as implemented⁴⁶ in MOLPRO at each separation, using the quadruple- ζ and



quintuple- ζ basis sets as described. The spin-orbit calculation employed state-averaged complete-active space self-consistent field (SA-CASSCF) wavefunctions of the lowest $^2\Pi$ and $^2\Sigma^+$ states. In the latter calculations, for Si^+ -RG, the following orbitals were frozen (*i.e.* doubly occupied and not optimized): $\text{Si}^+(1s2s2p)$; Kr (3s3p3d); Xe (4s4p4d); Rn (5s5p5d). For Ge^+ -RG (RG = Ar-Rn), the following orbitals were frozen: Ge (3s3p); Ar(1s2s2p); Kr (3s3p); Xe (4s4p); Rn (5s5p), while for Ge^+ -RG (RG = He and Ne), all orbitals outside of the ECP were included in the correlation treatment. Finally, both the spin-orbit and non-spin-orbit CP-corrected interaction potentials were point-by-point extrapolated to the basis set limit utilizing the two-point (cubic) formula of Halkier *et al.*^{47,48} at each separation; these final potentials are denoted $\text{RCCSD(T)/aV}\infty\text{Z}$.

We note that the ECP and basis sets for Ge and RG atoms have been tested thoroughly in the original studies.^{44,45} In addition, we experimented with the frozen orbitals, with the active spaces indicated above being those that ensured all orbitals remained as either correlated or not in the calculations; in particular, we observed that there was sometimes energetic overlap between the M^+ and RG atomic orbitals, and in such cases, the active space had to be expanded to include all such orbitals; failure to do so led to discontinuities in the potential energy curves at certain internuclear separations. The core electrons are not expected to contribute to the relatively weak interactions covered in the present work.

Potentials were calculated with default convergence thresholds in MOLPRO, except for the Ge^+ -He and Ge^+ -Ne potentials, where the convergence was tightened to ensure smooth curves over a wide-enough range, with convergence of the energy to $10^{-12} E_h$, orbitals in the SCF program to 10^{-8} and the CCSD coefficients to 10^{-7} . For all systems, at the longest R values, the curves lost their smoothness; as a consequence, we omit the data for these regions in the reported potentials – see ESI.†

It is generally accepted that T_1 diagnostic values <0.02 indicate that there is little multireference character in the CCSD electronic wavefunction.⁴⁹ In the present case, they are <0.02 for all except a small number of cases, which were localized to the $^2\Sigma^+$ state, where values crept above this value high on the repulsive wall (generally <0.04). This is not expected to affect the calculated spectroscopic parameters, and will only affect the ion transport properties at temperatures much higher than those that are used experimentally. We do note, however, that the spin-orbit splittings of the $^2\Pi_\Omega$ states (see Section 3.2) are supportive of some charge transfer in these complexes.

Population analyses were carried out for the $\text{X}^2\Pi$ state at the R_e value determined from the $\text{RCCSD(T)/aV}\infty\text{Z}$ potential, using standard Mulliken population analysis. Additionally, we used the NBO program⁵⁰ embedded in Gaussian 16⁵¹ to undertake a natural population analysis (NPA) for each of the complexes. Charge analyses were also undertaken with Bader's atoms-in-molecules (AIM) method, employing the program AIMAll.⁵² In all cases, triple- ζ quality versions of the basis sets employed for the potential energy curves above were used, and the QCISD density (from Gaussian 16) was employed for the NPA and AIM analyses.

Rovibrational energy levels were obtained from the calculated $\text{RCCSD(T)/aV}\infty\text{Z}$ interaction potentials using the LEVEL

program.⁵³ The lowest two relevant levels were used in each case to obtain the spectroscopic constants from standard formulae. We calculated these for $^{28}\text{Si}^+$ and $^{74}\text{Ge}^+$ with the most abundant, naturally-occurring RG isotope in each case.

2.2 Transport coefficients

We calculated the transport cross sections for Si^+ and Ge^+ travelling through a bath of each RG from the respective $\text{RCCSD(T)/aV}\infty\text{Z}$ *ab initio* interaction potential energy curves as functions of the ion-neutral collision energy using the classical-mechanical program PC⁵⁴ that is an improved version of the earlier program QVALUES.^{55,56} The cross sections converged within 0.05% in all cases. The range of collision energies covered was from $1 \times 10^{-9} E_h$ to the energy calculated at the smallest internuclear separation, always above $1 E_h$, depending on the system. Only the potentials of the spin-orbit states were considered for these calculations.

The cross sections as a function of collision energy were used in the Gram-Charlier program GC^{55,57,58} to determine the reduced mobility, K_0 , and the other gaseous ion transport coefficients as functions of E/n_0 (the ratio of the electric field to the gas number density) at gas temperatures, T , of 100, 200, 300, 400 and 500 K for all species, and additionally 4.35 K for systems containing He. The range of E/n_0 covered was 0.01–1000 Td ($1 \text{ Td} = 10^{-21} \text{ V m}^2$). We also used program VARY⁵⁹ to determine the zero-field values of the mobility and the ion diffusion coefficient as a function of T from 0.001 to 10 000 K. Calculations were performed separately for all of the naturally-occurring isotopes for each cation, while each RG was assumed to be composed of the naturally-occurring mixture of isotopes. The calculated mobilities are generally precise to within the precision of the cross sections at E/n_0 values below 20 Td. The results are progressively less precise as E/n_0 increases to 1000 Td. These details, as well as the mobilities and other transport properties, can be obtained from the tables placed in an online database.⁶⁰ The accuracy of the calculated mobilities is the same as the reported precision if the interaction potentials are correct; owing to the possible errors in these (see below), we expect the transport properties to be accurate only within 5%.

For cations in the $^2P_{1/2}$ state, the cross-sections were calculated from the $^2\Pi_{1/2}$ potential, while for the $^2P_{3/2}$ state, cross-sections were obtained as a 1 : 1 weighting of those arising from the $^2\Pi_{3/2}$ and $^2\Sigma_{1/2}^+$ potentials. In addition, we also undertook calculations for the case where both spin-orbit states were present with equal concentrations, these “averaged spin-orbit” values are denoted ASO and arise from a 1 : 1 : 1 weighting of the cross-sections arising from the three spin-orbit states.

Additionally, for the transport calculations, each spin-orbit interaction potential was shifted such that the interaction energies merged smoothly with the appropriate $1/R^4$ ion-induced dipole interaction energy at 30 Å. This was done to avoid round-off errors that could prevent the transport cross sections from smoothly approaching the ion/induced-dipole values that are correct at zero energy for the transport cross sections.



3. Results and discussion

3.1 Spectroscopic constants for $\text{Si}^+\text{-RG}$ and $\text{Ge}^+\text{-RG}$

All of the calculated spin-orbit and non-spin-orbit RCCSD(T)/ $aV\infty Z$ potentials are presented in the ESI.†

Portions of these potentials, showing the regions around the potential energy minima, are shown in Fig. 1 for $\text{Si}^+(^2P)\text{-RG}$

(RG = He–Rn). The potentials for $\text{Si}^+\text{-RG}$ (RG = He–Ar) were shown and discussed in ref. 38, and an analysis of the spectroscopic constants was given therein. (The $\text{Si}^+\text{-RG}$ potential data were not given in ref. 38 for RG = He–Ar, and so they are included in the ESI† herein, for completeness.) Similarly, portions of the calculated non-spin-orbit and spin-orbit RCCSD(T)/ $aV\infty Z$ potentials are shown in Fig. 2 for $\text{Ge}^+(^2P)\text{-RG}$ (RG = He–Rn).

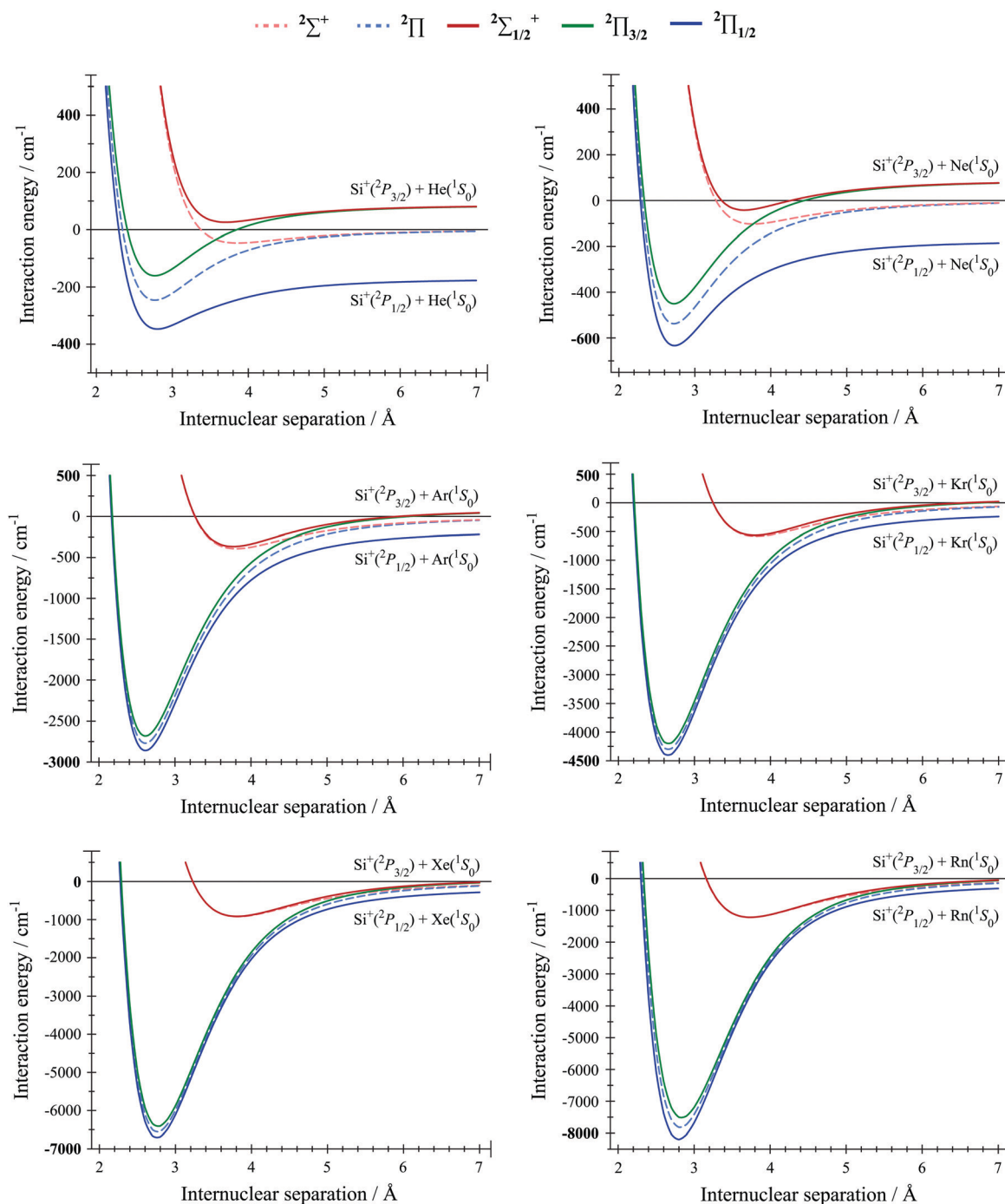


Fig. 1 Potential energy curves calculated for Si^+ interacting with each RG (RG = He–Rn). Note that the ordinate scales are not the same for all plots. The legend at the top of the figure applies to all plots. The interaction energies have been calculated as a function of the internuclear separation at the RCCSD(T)/ $aV\infty Z$ level of theory (see text for details). We show both the non-spin-orbit and spin-orbit curves, as dashed and solid lines, respectively, and these are discussed further in the text.



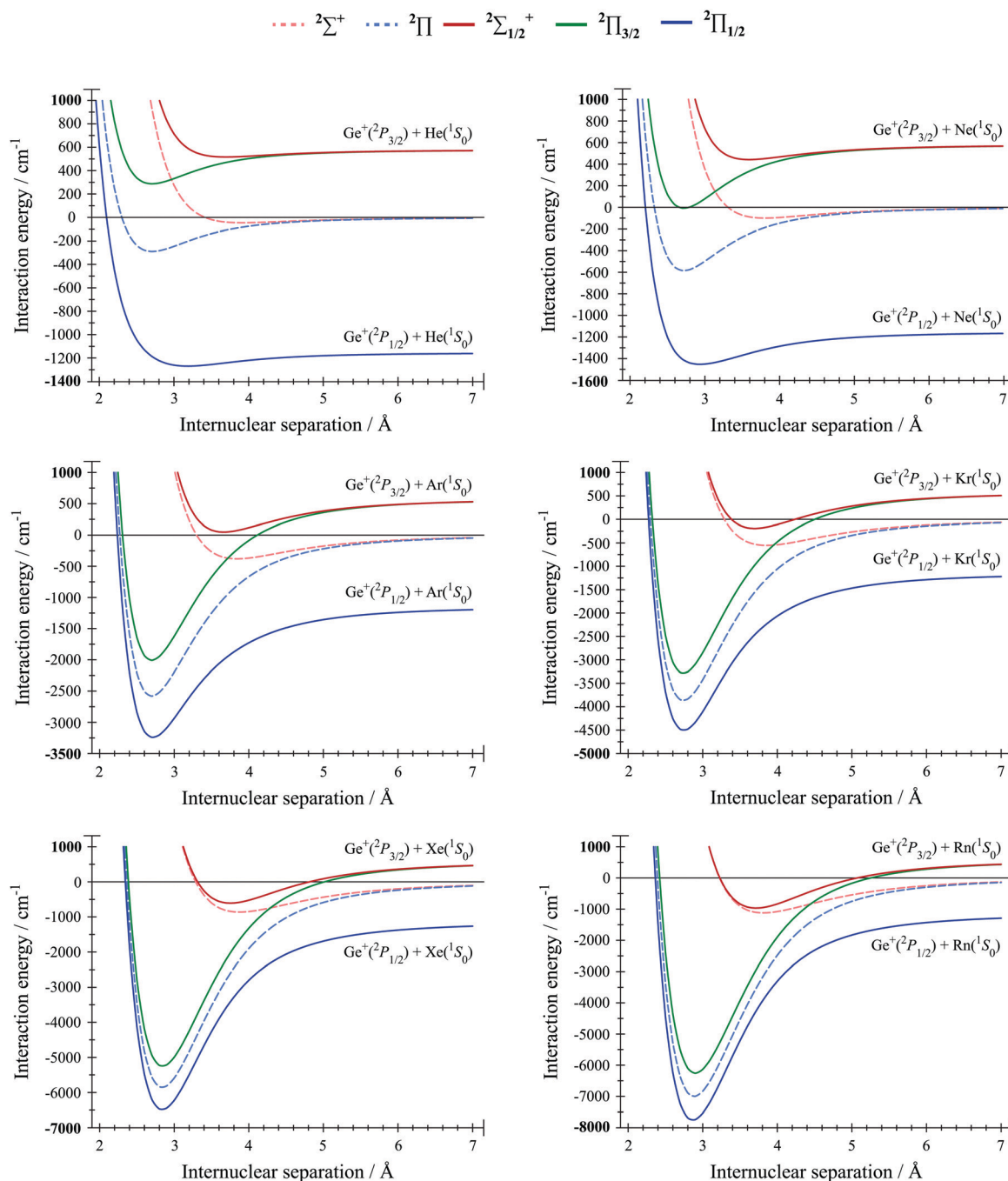


Fig. 2 Potential energy curves calculated for Ge^+ interacting with each RG (RG = He–Rn). Note that the ordinate scales are not the same for all plots. The legend at the top of the figure applies to all plots. The interaction energies have been calculated as a function of the internuclear separation at the RCCSD(T)/ $aV\infty Z$ level of theory (see text for details). We show both the non-spin-orbit and spin-orbit curves, as dashed and solid lines, respectively, and these are discussed further in the text.

The calculated values for the atomic cation spin-orbit separation of the $^2P_{3/2}$ and $^2P_{1/2}$ states were 256.5 cm^{-1} for Si^+ , which compares well to the experimental value³⁹ of 287.24 cm^{-1} . For Ge^+ , we calculate values of 1724 cm^{-1} (RG = Ar–Rn), while a value of 1734 cm^{-1} was obtained for RG = He and Ne, where tighter convergence criteria were employed. For those latter calculations, all non-ECP orbitals of Ge^+ were included in the SA-CASSCF procedure used to generate the wavefunctions for

the spin-orbit calculations – these compare well to the experimental value of 1767.36 cm^{-1} .³⁹ The agreement is good enough for our purposes, with the differences likely arising from higher-order interactions than those treated here, basis set incompleteness, and also the neglect of inclusion of higher-energy spin-orbit states.

From the plots in Fig. 1 and 2, it can be seen that the $X^2\Pi$ states are always much more strongly bound than are the $A^2\Sigma^+$



ones. For the $^2\Pi$ state, the unpaired electron is positioned perpendicular to the internuclear axis, so allowing the RG atom to get closer to, and hence to interact more strongly with, the positive charge located on Si^+ or Ge^+ . Similar observations were made for the C^+-RG complexes (see ref. 26 and 37). The resultant equilibrium position arises from a balance of electrostatic attractive and repulsive interactions, as well as Pauli repulsion and has been discussed by Bellert and Breckenridge in ref. 61. The spectroscopic constants obtained from the non-spin-orbit interaction potentials are presented in Table 1 for Si^+-RG and in Table 2 for Ge^+-RG ; for the former, we have included the values from ref. 38 for Si^+-RG ($\text{RG} = \text{He}-\text{Ar}$), for comparison.

Below, we shall comment on the trends in four of the key parameters. Once spin-orbit interaction is included, then we see significant changes in the parameters for the $^2\Sigma_{1/2}^+$ and $^2\Pi_{1/2}$ states, when compared to the corresponding non-spin-orbit states, with the $^2\Sigma_{1/2}^+$ state generally becoming more-strongly bound, and the $^2\Pi_{1/2}$ state generally becoming more-weakly bound, owing to the mixing between these same- Ω states. Here, we expect the parameters for the $^2\Pi_{3/2}$ state to be the same as for the $^2\Pi$ state, since there are no other $\Omega = 3/2$

states with which to interact, and this is largely the case for $\text{RG} = \text{He}-\text{Ar}$, but with small deviations occurring for the cases with the heavier RG, particularly for Si^+-RG . Such deviations were also seen for C^+-RG ,³⁷ and are commented on later.

For the non-spin-orbit potentials, we first consider the trends in R_e , which are presented graphically in Fig. 3. For each of Si^+-RG and Ge^+-RG , the trends are not monotonically increasing with the atomic number of RG, as might have been expected from their increasing radius. This is due to a balance of that trend with the increasing strength of interaction, arising from the concomitant increase of the polarizability of the RG atom. As a consequence of this balance, the R_e values for the $^2\Pi$ states of Si^+-RG slightly decrease before increasing, while for Ge^+-RG the values are almost constant initially, before rising. Thus, for the $^2\Pi$ states, we conclude that the size of the RG atom eventually dominates R_e for the gases with higher atomic numbers, outweighing the effect of the increasing polarizability. The trends are similar, but not identical, for the $^2\Sigma^+$ states, with notably a small dip in the value of R_e between $\text{RG} = \text{Xe}$ and Rn for both Si^+-RG and Ge^+-RG , emphasising the subtle balance between the aforementioned factors. In contrast, for both the $^2\Pi$ and $^2\Sigma^+$ states, the D_e values are dominated by the increasing RG

Table 1 Spectroscopic constants for $^{28}\text{Si}^+(^2P_j)-\text{RG}(^1S_0)$ ($\text{RG} = \text{He, Ne, Ar, Kr, Xe, Rn}$) at the RCCSD(T)/ $aV\infty Z$ level^a

State	$R_e/\text{\AA}$	D_e/cm^{-1}	D_0/cm^{-1}	ω_e/cm^{-1}	$\omega_e x_e/\text{cm}^{-1}$	$k/\text{N m}^{-1}$	B_e/cm^{-1}	α/cm^{-1}	Ref.
Si^+-He									
$^2\Pi_{1/2}$	2.803	175	131	97.3	17.36	1.95	0.6128	1.084×10^{-1}	38
$^2\Pi_{3/2}$	2.769	246	193	112.5	13.93	2.61	0.6279	7.887×10^{-2}	38
$^2\Pi$	2.769	246	193	112.5	13.93	2.61	0.6279	7.920×10^{-2}	38
$^2\Sigma_{1/2}^+$	3.703	60	38	49.5	11.93	0.51	0.3511	8.477×10^{-2}	38
$^2\Sigma^+$	3.861	46	29	40.4	10.19	0.34	0.3229	8.374×10^{-2}	38
Si^+-Ne									
$^2\Pi_{1/2}$	2.732	459	415	90.3	4.947	5.60	0.1937	9.743×10^{-3}	38
$^2\Pi_{3/2}$	2.724	538	492	93.1	4.333	5.96	0.1948	9.006×10^{-3}	38
$^2\Pi$	2.724	538	492	93.1	4.332	5.96	0.1948	9.002×10^{-3}	38
$^2\Sigma_{1/2}^+$	3.648	129	110	40.7	4.104	1.14	0.1086	9.248×10^{-3}	38
$^2\Sigma^+$	3.763	103	87	33.6	3.444	0.78	0.1021	9.387×10^{-3}	38
Si^+-Ar									
$^2\Pi_{1/2}$	2.611	2686	2603	167.9	2.585	27.3	0.1503	2.492×10^{-3}	38
$^2\Pi_{3/2}$	2.611	2770	2686	168.1	2.572	27.4	0.1503	2.574×10^{-3}	38
$^2\Pi$	2.611	2771	2687	168.1	2.573	27.4	0.1503	2.492×10^{-3}	38
$^2\Sigma_{1/2}^+$	3.767	455	427	55.2	1.784	2.95	0.07219	2.207×10^{-3}	38
$^2\Sigma^+$	3.803	394	369	50.5	1.872	2.48	0.07083	2.453×10^{-3}	38
Si^+-Kr									
$^2\Pi_{1/2}$	2.651	4237	4146	183.4	1.880	41.6	0.1143	1.289×10^{-3}	Present work
$^2\Pi_{3/2}$	2.656	4290	4200	182.6	1.874	41.2	0.1139	1.293×10^{-3}	Present work
$^2\Pi$	2.654	4307	4216	183.0	1.871	41.4	0.1141	1.199×10^{-3}	Present work
$^2\Sigma_{1/2}^+$	3.792	652	625	54.7	1.188	3.70	0.05588	1.268×10^{-3}	Present work
$^2\Sigma^+$	3.812	582	556	51.9	1.306	3.33	0.05529	1.370×10^{-3}	Present work
Si^+-Xe									
$^2\Pi_{1/2}$	2.756	6541	6439	202.9	1.408	56.0	0.09616	7.313×10^{-4}	Present work
$^2\Pi_{3/2}$	2.768	6502	6402	200.6	1.395	54.7	0.09532	7.557×10^{-4}	Present work
$^2\Pi$	2.762	6563	6462	201.7	1.402	55.3	0.09574	7.717×10^{-4}	Present work
$^2\Sigma_{1/2}^+$	3.809	1002	972	61.2	1.077	5.09	0.05034	8.569×10^{-4}	Present work
$^2\Sigma^+$	3.816	913	892	59.9	1.156	4.88	0.05016	9.341×10^{-4}	Present work
Si^+-Rn									
$^2\Pi_{1/2}$	2.795	8026	7921	210.3	1.214	64.8	0.08685	6.210×10^{-4}	Present work
$^2\Pi_{3/2}$	2.835	7607	7506	201.7	1.173	59.6	0.08442	5.874×10^{-4}	Present work
$^2\Pi$	2.817	7823	7721	205.0	1.178	61.5	0.08550	6.201×10^{-4}	Present work
$^2\Sigma_{1/2}^+$	3.737	1306	1272	67.4	1.117	6.44	0.04858	8.137×10^{-4}	Present work
$^2\Sigma^+$	3.737	1219	1186	66.6	1.164	6.50	0.04858	8.113×10^{-4}	Present work

^a Symbols in the headers have their usual spectroscopic meaning. See text for further details, as well as a discussion of the trends in these values – see also Fig. 3. Spin-orbit states are labelled with their Ω quantum number, while non-spin-orbit states have no Ω quantum number given.



Table 2 Spectroscopic constants for $^{74}\text{Ge}^+(^2P_J)\text{-RG}(^1S_0)$ (RG = He, Ne, Ar, Kr, Xe, Rn) at the RCCSD(T)/aV ∞ Z level^a

State	$R_e/\text{\AA}$	D_e/cm^{-1}	D_0/cm^{-1}	ω_e/cm^{-1}	$\omega_e x_e/\text{cm}^{-1}$	$k/\text{N m}^{-1}$	B_e/cm^{-1}	α/cm^{-1}
Ge⁺-He								
$^2\Pi_{1/2}$	3.183	113	86	59.6	8.273	0.79	0.4382	6.170×10^{-2}
$^2\Pi_{3/2}$	2.706	289	232	122.4	14.07	3.35	0.6063	6.937×10^{-2}
$^2\Pi$	2.708	288	231	122.1	14.07	3.33	0.6054	6.937×10^{-2}
$^2\Sigma_{1/2}^+$	3.695	60	40	45.5	10.04	0.46	0.3252	7.266×10^{-2}
$^2\Sigma^+$	3.916	44	28	37.2	9.107	0.31	0.2895	7.218×10^{-2}
Ge⁺-Ne								
$^2\Pi_{1/2}$	2.933	297	273	49.3	2.261	2.26	0.1245	7.221×10^{-3}
$^2\Pi_{3/2}$	2.718	586	544	87.5	3.523	7.10	0.1450	5.661×10^{-3}
$^2\Pi$	2.719	585	543	87.4	3.518	7.09	0.1449	5.552×10^{-3}
$^2\Sigma_{1/2}^+$	3.590	136	119	34.8	2.817	1.12	0.08312	5.999×10^{-3}
$^2\Sigma^+$	3.802	100	86	28.1	2.476	0.73	0.07411	5.797×10^{-3}
Ge⁺-Ar								
$^2\Pi_{1/2}$	2.714	2091	2029	125.2	1.954	24.0	0.08823	1.359×10^{-3}
$^2\Pi_{3/2}$	2.697	2581	2515	132.6	1.743	26.9	0.08935	1.212×10^{-3}
$^2\Pi$	2.698	2580	2514	132.3	1.742	26.8	0.08928	1.197×10^{-3}
$^2\Sigma_{1/2}^+$	3.660	531	506	50.7	1.474	3.92	0.04852	1.243×10^{-3}
$^2\Sigma^+$	3.843	380	361	39.3	1.187	2.37	0.04400	1.225×10^{-3}
Ge⁺-Kr								
$^2\Pi_{1/2}$	2.746	3352	3290	125.4	1.150	36.4	0.05689	5.148×10^{-4}
$^2\Pi_{3/2}$	2.740	3861	3797	128.8	1.066	38.4	0.05714	4.920×10^{-4}
$^2\Pi$	2.739	3867	3803	128.7	1.066	38.4	0.05718	4.979×10^{-4}
$^2\Sigma_{1/2}^+$	3.692	772	748	47.9	0.8615	5.32	0.03147	5.096×10^{-4}
$^2\Sigma^+$	3.856	554	535	37.0	0.7123	3.17	0.02885	5.216×10^{-4}
Ge⁺-Xe								
$^2\Pi_{1/2}$	2.838	5338	5271	133.8	0.7588	50.0	0.04418	2.418×10^{-4}
$^2\Pi_{3/2}$	2.842	5824	5757	134.9	0.7273	50.8	0.04406	2.571×10^{-4}
$^2\Pi$	2.838	5859	5791	135.2	0.7289	51.0	0.04418	2.544×10^{-4}
$^2\Sigma_{1/2}^+$	3.752	1186	1161	51.0	0.5633	7.25	0.02528	2.564×10^{-4}
$^2\Sigma^+$	3.874	863	843	40.4	0.5421	4.55	0.02371	3.253×10^{-4}
Ge⁺-Rn								
$^2\Pi_{1/2}$	2.865	6605	6539	133.5	0.5997	58.2	0.03703	2.088×10^{-4}
$^2\Pi_{3/2}$	2.899	6831	6766	130.3	0.5632	55.5	0.03617	1.864×10^{-4}
$^2\Pi$	2.883	7003	6937	132.1	0.5675	57.0	0.03657	1.904×10^{-4}
$^2\Sigma_{1/2}^+$	3.714	1546	1520	52.5	0.4271	8.99	0.02204	1.738×10^{-4}
$^2\Sigma^+$	3.810	1120	1099	42.5	0.4731	5.89	0.02094	2.393×10^{-4}

^a Values all obtained in the present work. Symbols in the headers have their usual spectroscopic meaning. See text for further details, as well as a discussion of the trends in these values – see also Fig. 3. Spin-orbit states are labelled with their Ω quantum number, while non-spin-orbit states have no Ω quantum number given.

polarizability throughout. Similar, but not identical, trends are seen for the $^2\Pi$ and $^2\Sigma^+$ states, with the $^2\Sigma^+$ state being more weakly bound and with a significantly longer R_e values in all cases, in line with the orientation of the unpaired valence p electron, as mentioned previously.

The trends in ω_e are also non-monotonic, but this time it is the increasing mass of the RG atom that counteracts the increasing strength of interaction: once the mass effect is removed by calculating the force constants, the trends in k are very similar to those of D_e , as expected – see Fig. 3. Again, there are similar, but slightly different trends observed for the $^2\Pi$ and $^2\Sigma^+$ states, with the $^2\Sigma^+$ state having a significantly smaller ω_e value in all cases, and a lower k value, in line with the weaker interaction.

We have also used the LEVEL program⁵³ to calculate the bound vibrational levels for both the spin-orbit and non-spin-orbit potentials, and these are presented in the ESI†. In Fig. 4 and 5, for both the $^2\Sigma^+$ and $^2\Pi$ states, we plot the vibrational energy level spacings against $v + 1$ (Birge-Sponer-like plots), for all $\text{Si}^+\text{-RG}$ and $\text{Ge}^+\text{-RG}$ complexes, except for $\text{RG} = \text{He}$, where there were very few bound levels (see ESI†). On these diagrams,

the solid straight line represents the expected trend for levels obeying the vibrational energy expression arising from the Morse potential, truncated at the quadratic term, with values of ω_e and $\omega_e x_e$ obtained from the lowest two vibrational energy levels (these values are given in Tables 1 and 2). It can be seen in all cases that the lower v values follow this line closely, but that there are significant deviations later on. Further, at the highest v levels, which correspond to the long- R regions of the potential, where charge/induced-dipole interactions are dominant, the trend is expected to follow LeRoy-Bernstein behaviour.^{62–64} This long-range behaviour is expected to follow a $(\Delta G_{v+1/2})^{2n/(n+2)}$ dependence, where n is that of the R^{-n} dependence of the potential at long range, *i.e.* the leading term in the interaction potential. For an atomic cation/rare gas interaction, an R^{-4} dependence is expected, and so we expect a $(\Delta G_{v+1/2})^{4/3}$ dependence in the Birge-Sponer plots close to the dissociation limit. These overall expectations are largely met by the $^2\Sigma^+$ plots for both $\text{Si}^+\text{-RG}$ and $\text{Ge}^+\text{-RG}$. For the $^2\Pi$ states, in the intermediate regions the calculated energies of the vibrational levels dip below this line, most noticeably for the heavier RG atoms. Approaching from larger R , corresponding to the



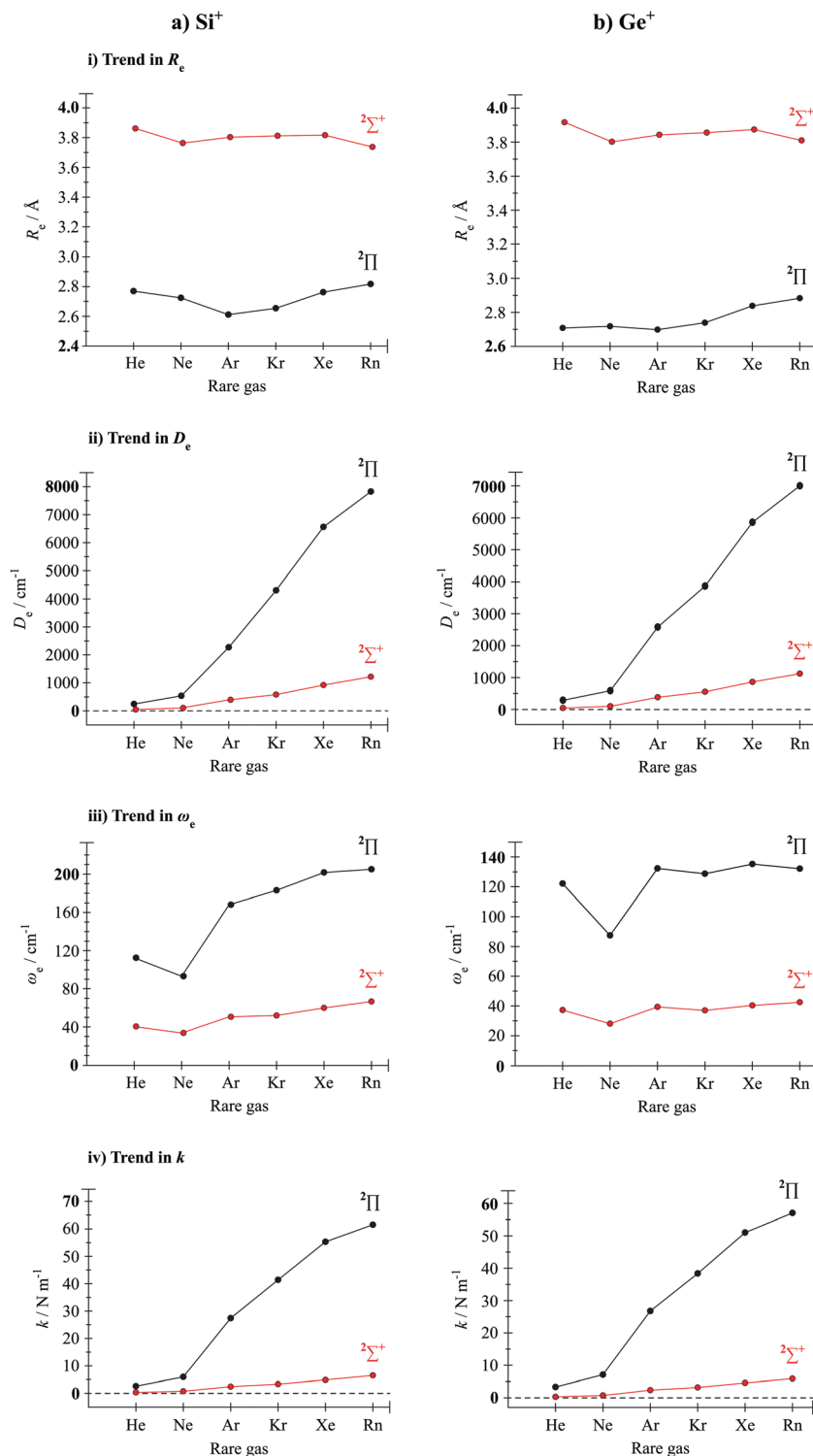


Fig. 3 Trends in calculated R_e , D_e , ω_e and k for the $2\Sigma^+$ and 2Π states of (a) Si^+ -RG and (b) Ge^+ -RG as a function of RG – see text for further discussion. Note that the ordinate scales are not the same for all plots.

high- ν levels, the implication is that the interaction potential in the intermediate region initially softens compared to that close to the minimum, as a result of electron density movement away from the internuclear region, for example partial hybridization,³⁵ however, gradually the increasing cost of this cannot be

met from the decrease in repulsion, and the curvature of the potential changes. Close to R_e , there is also the possibility of partial charge transfer, and some further insight into the latter is obtained from the calculated charges and $H(R)$ parameter, discussed in the following subsection.



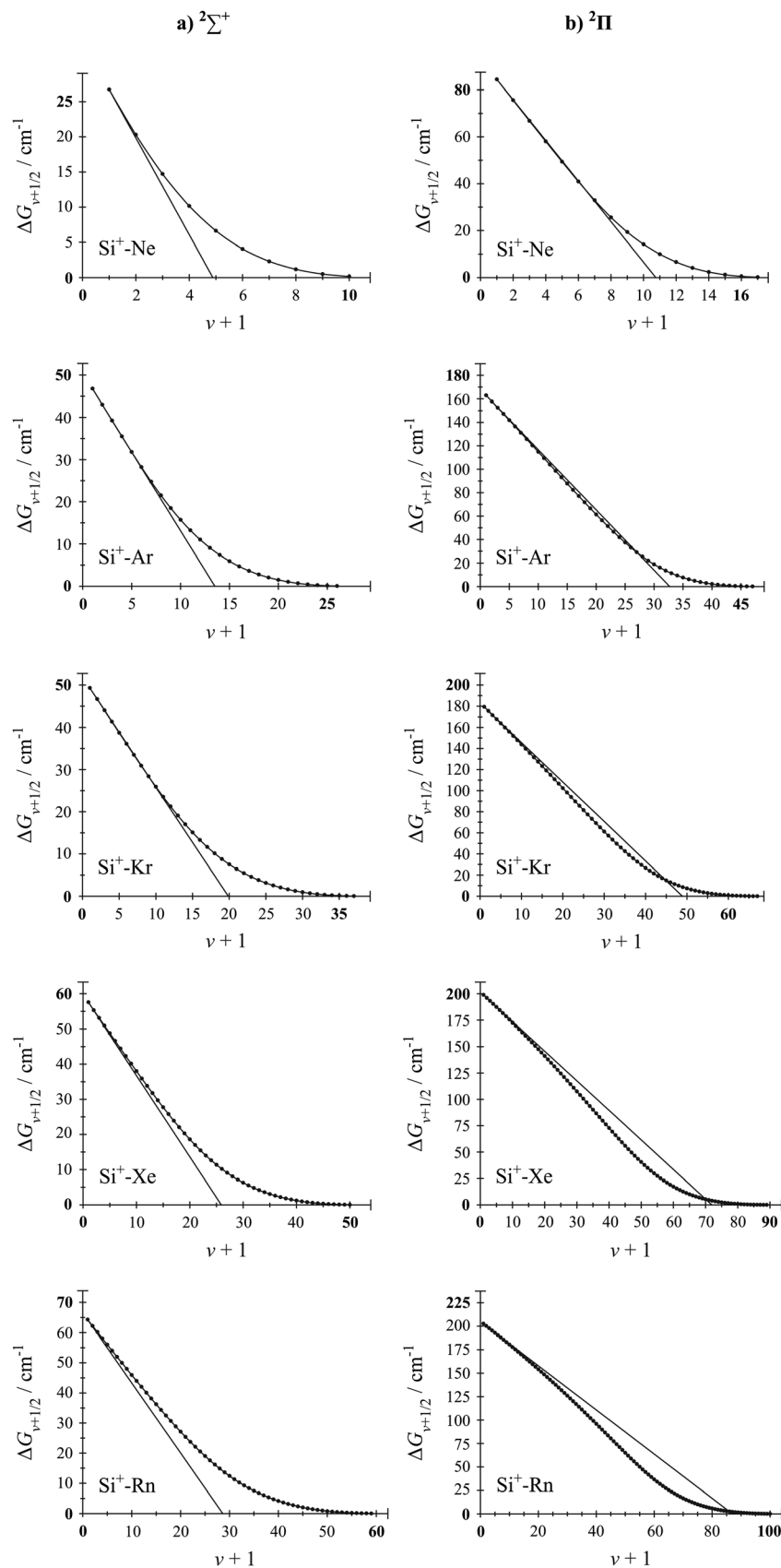


Fig. 4 Birge–Sponer-like plots for the (a) $2\Sigma^+$ and (b) 2Π states of $\text{Si}^+ - \text{RG}$ constructed from the calculated vibrational energy spacings obtained from the RCCSD(T)/ $aV \infty Z$ potentials. The solid lines are obtained from the ω_e and $\omega_e x_e$ values reported in Table 1 and are obtained from the lowest two vibrational energy levels and D_e . Note that the ordinate and abscissa scales are not the same for all plots. (Values for $\text{RG} = \text{He}$ are not plotted since there are only very few calculated values – see text and ESI†)



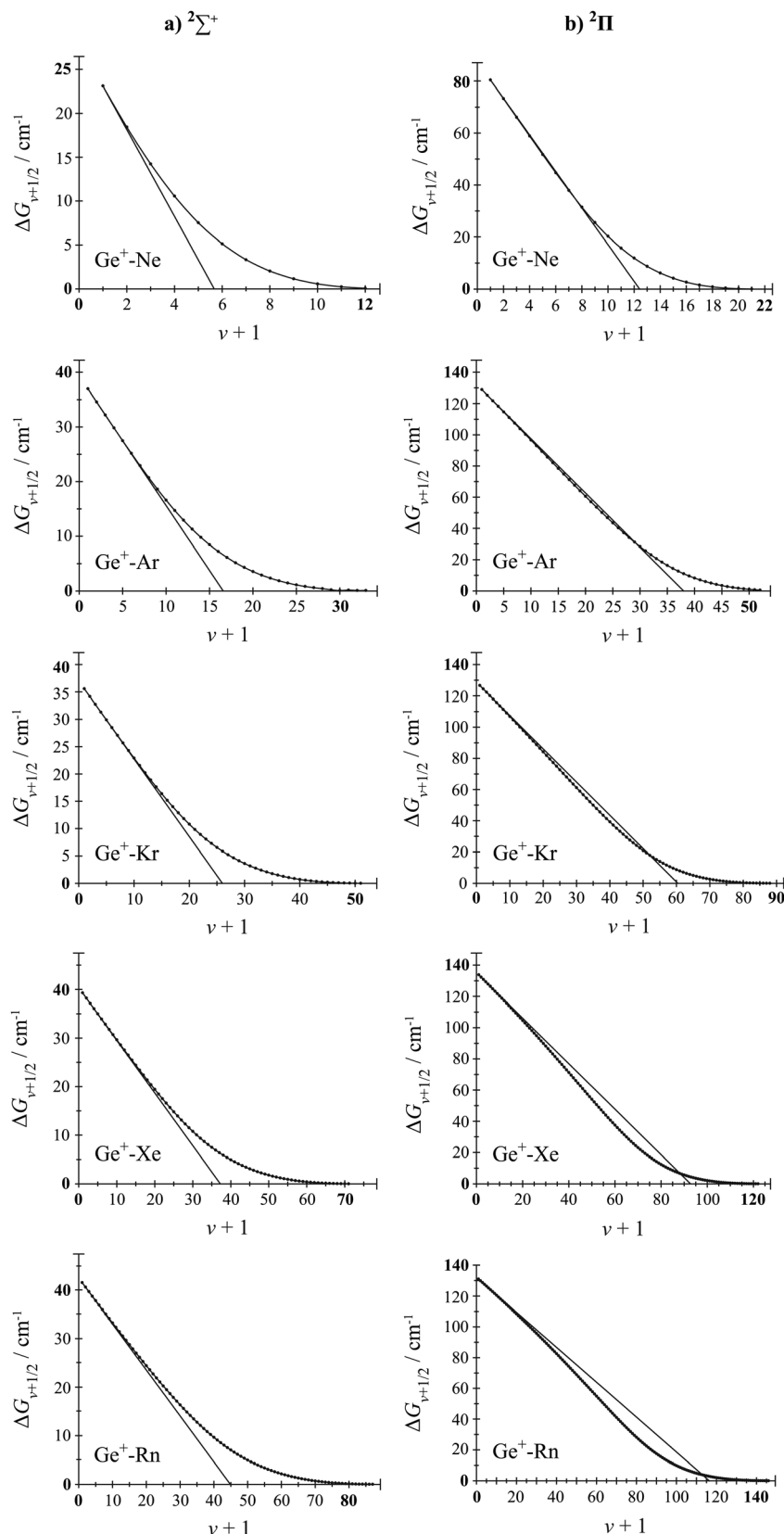


Fig. 5 Birge-Sponer-like plots for the (a) $2\Sigma^+$ and (b) 2Π states of $\text{Ge}^+ - \text{RG}$ constructed from the calculated vibrational energy spacings obtained from the RCCSD(T)/aV ∞ Z potentials. The solid lines are obtained from the ω_e and $\omega_e x_e$ values reported in Table 2 and are obtained from the lowest two vibrational energy levels and D_e . Note that the ordinate and abscissa scales are not the same for all plots. (Values for RG = He are not plotted since there are only very few calculated values – see text and ESI.†)



3.2 Charges and chemical bonding

The calculated values for the local energy parameter, $H(R)$,⁶⁵ evaluated at the bond critical point, are presented in Table 3, with negative $H(R)$ values suggested as indicating that there is a chemical bonding contribution, based upon observations for known covalent molecules. (It has been argued in ref. 65 that this parameter is more reliable than the deformation electron density, owing to the difficulty of defining a reference density; however, definitive methods of establishing criteria for chemical interactions are still not available, and as such, $H(R)$ must be viewed as a qualitative parameter, rather than a quantitative one.) The values suggest that the cases involving He and Ne show essentially no chemical bonding, while some contribution from such may be present for RG = Ar–Rn. Similarly, the NPA and AIM calculated charges are in line with this interpretation, suggesting some charge transfer from $M^+ \rightarrow RG$. Thus, we infer that, at R values approaching R_e , some charge transfer may be occurring, which would increase the interaction above that expected from a neutral atom interacting with an atomic cation. As is well-known, Mulliken charges are often unreliable, and the close agreement between the NPA and AIM charges here, and the fact that they are discrepant with the Mulliken charges confirms this in the present case. We hypothesise that the Mulliken analyses are misattributing the electron density, owing to the large size of the RG atom, and also the “embedding” of the cation into the region where the RG density would be expected – see ref. 37 for orbital contour plots that show this effect for C^+RG .

Table 3 Calculated charges and $H(R)$ values^a

M	RG	$q(M)$			$q(RG)$			$H(R)^b$
		Mulliken	NPA	AIM	Mulliken	NPA	AIM	
C	He	1.00	0.99	0.99	0.00	0.01	0.01	2.5×10^{-3}
	Ne	0.96	0.97	0.97	0.04	0.03	0.03	2.5×10^{-3}
	Ar	0.57	0.67	0.71	0.43	0.33	0.29	-4.5×10^{-2}
	Kr	0.53	0.53	0.57	0.47	0.47	0.43	-4.6×10^{-2}
	Xe	0.10	0.34	0.38	0.90	0.66	0.62	-4.7×10^{-2}
Si	He ^c	1.00	1.00	1.00	0.00	0.00	0.00	1.4×10^{-3}
	Ne ^c	0.98	0.99	1.00	0.02	0.01	0.00	3.1×10^{-4}
	Ar ^c	0.93	0.91	0.95	0.07	0.09	0.05	-6.7×10^{-3}
	Kr	0.84	0.85	0.91	0.16	0.15	0.09	-1.1×10^{-2}
	Xe	0.67	0.75	0.83	0.33	0.25	0.17	-1.4×10^{-2}
Ge	Rn	0.57	0.71	0.78	0.43	0.29	0.22	-1.5×10^{-2}
	He	1.01	1.00	1.00	-0.01	0.00	0.00	1.7×10^{-3}
	Ne	0.98	0.99	1.00	0.02	0.01	0.00	9.3×10^{-4}
	Ar	0.96	0.93	0.95	0.04	0.07	0.05	-2.2×10^{-3}
	Kr	0.89	0.88	0.91	0.11	0.12	0.09	-5.5×10^{-3}
	Xe	0.74	0.79	0.83	0.26	0.21	0.17	-8.1×10^{-3}
	Rn	0.66	0.74	0.78	0.34	0.26	0.22	-8.9×10^{-3}

^a Values are from Mulliken population analysis, natural population analysis (NPA) and Bader's atoms-in-molecules (AIM) approach – see text for further details and comments. Calculations were performed at the R_e values reported in ref. 36 and 37 for C^+RG , and in Tables 1 and 2 for Si^+RG (RG = Kr–Rn) and Ge^+RG , respectively. ^b The $H(R)$ parameter is described in ref. 65 and is evaluated at the bond critical point: a negative value indicates an element of chemical bonding. ^c Values for Si^+RG (RG = He–Ar) are undertaken as part of the work reported in ref. 38, but were not reported therein.

This charge transfer was discussed in depth in ref. 37 for C^+RG , where multireference configuration interaction (MRCI) calculations were also undertaken. These confirmed the role of charge transfer in these systems. The RCCSD(T) method, employed in the present calculations, is a single-reference method but the T_1 diagnostic values (see above) suggest that this is mostly adequate for the present cases. We do not report any MRCI calculations in the present work, although we would expect the results to be similar to those for C^+RG .³⁷

Further insight into the interaction can be obtained by examining the spin-orbit splitting between the minima of the $^2\Pi_{1/2}$ and $^2\Pi_{3/2}$ states (see Tables 4 and 5) and comparing that to the splitting at the dissociation asymptotes. In the latter case, we expect the splitting to be that of the atomic cation states, $^2P_{1/2}$ and $^2P_{3/2}$ that, as we noted earlier, have experimental values³⁹ of 287.24 cm^{-1} for Si^+ , and 1767.36 cm^{-1} for Ge^+ , with the calculated asymptotic spin-orbit splittings being 256.5 cm^{-1} , and 1724 cm^{-1} or 1734 cm^{-1} , respectively. (The calculated splittings between the $^2\Pi_{1/2}$ and $^2\Pi_{3/2}$ states are given in Tables 4 and 5.)

If the interaction is significant, we expect the spin and orbital angular momenta to couple to the internuclear axis, and for Hund's case (a) behaviour to be seen. The evolution from Hund's case (a) to Hund's case (c) has been discussed in ref. 66 for $\dots p^1$ excited states of Au–RG complexes. In such cases, the splitting at the minima would be expected to be $2/3$ that at the asymptote, in the absence of other interactions. In ref. 36 we discussed this for C^+RG (RG = He–Xe), noting that the expectation was well exhibited for C^+He and C^+Ne , but that the splitting swiftly rose as the atomic number of the RG atom increased, becoming over ten times the expected splitting for C^+Xe , consistent with involvement of RG^+ in determining the value.

For Si^+RG , it can be seen that a similar scenario unfolds (Table 4), but now the differences to the expected splitting are much less, becoming “only” just less than four times as large for Si^+Rn . This indicates that the role of charge transfer is significantly less for the Si^+RG complexes, in line with the calculated AIM and NPA charges (Table 3). This trend continues for Ge^+RG , where now the calculated splittings in the Ge^+RG complexes are almost precisely as expected for RG = Ar–Xe (Table 5), but slightly more for RG = Rn. It is interesting that for the lightest two RG atoms, He and Ne, where the interaction with the cation is weakest, the splitting is always slightly more than that expected. We interpret the latter as indicating that Hund's case (a) coupling is not quite complete. For RG = Ar, the splitting is close to that expected for Hund's case (a) coupling – whether this is wholly due to the presence of Hund's case (a) coupling, or a coincidence as the charge-transfer starts to turn on, is unclear.

The influence of the configuration mixing can also be seen in the spectroscopic constants. If we consider solely the spin-orbit states that arise from the $M^+(\dots ns^2np^1) + RG$ configuration, then, since there is only the one $\Omega = 3/2$ state, the $^2\Pi_{3/2}$ state should have precisely the same shape as the non-spin-orbit $^2\Pi$ state – it is merely shifted up in energy; hence, the spectroscopic



Table 4 Spin-orbit parameters for Si⁺–RG calculated at the RCCSD(T)/aV ∞ Z level – see text for details

	Si ⁺ –He	Si ⁺ –Ne	Si ⁺ –Ar	Si ⁺ –Kr	Si ⁺ –Xe	Si ⁺ –Rn
Calculated asymptotic splitting ($= 3/2\zeta^a/\text{cm}^{-1}$)	256.5	256.5	256.5	256.5	256.5	256.5
Predicted calculated Hund's case (a) splitting at R_e/cm^{-1}	171.0	171.0	171.0	171.0	171.0	171.0
Calculated $^2\Pi_{1/2} - ^2\Pi_{3/2}$ splitting at R_e^b/cm^{-1}	187.9	180.9	177.9	179.4	266.6	650.6
Actual/predicted splitting	1.10	1.06	1.04	1.05	1.56	3.81
IE (RG) ^c /eV	24.59	21.57	15.76	14.00	12.13	10.75
$^2P_{3/2} - ^2P_{1/2}$ splitting (RG ^d)/cm ⁻¹	n/a	780.4	1432	5370	10 537	30 895

^a ζ is the atomic spin-orbit splitting constant. ^b These are calculated at the R_e values of the $^2\Pi_{3/2}$ state reported in Table 1. ^c Accessing the lowest spin-orbit cationic state. ^d This is the experimental spin-orbit splitting for the ... np^5 ground electronic state configuration.³⁹

Table 5 Spin-orbit parameters for Ge⁺–RG calculated at the RCCSD(T)/aV ∞ Z level – see text for details

	Ge ⁺ –He	Ge ⁺ –Ne	Ge ⁺ –Ar	Ge ⁺ –Kr	Ge ⁺ –Xe	Ge ⁺ –Rn
Calculated asymptotic splitting ($= 3/2\zeta^a/\text{cm}^{-1}$)	1734	1734	1724	1724	1724	1724
Predicted calculated Hund's case (a) splitting at R_e/cm^{-1}	1156	1156	1149	1149	1149	1149
Calculated $^2\Pi_{1/2} - ^2\Pi_{3/2}$ splitting at R_e^b/cm^{-1}	1476	1406	1230	1194	1218	1465
Actual/predicted splitting	1.28	1.22	1.07	1.04	1.06	1.28
IE (RG) ^c /eV	24.59	21.57	15.76	14.00	12.13	10.75
$^2P_{3/2} - ^2P_{1/2}$ splitting (RG ^d)/cm ⁻¹	n/a	780.4	1432	5370	10 537	30 895

^a ζ is the atomic spin-orbit splitting constant. The values differ for RG = He, Ne from those of RG = Ar–Rn, owing to the correlation of different Ge⁺ electrons – see text for details. ^b These are calculated at the R_e values of the $^2\Pi_{3/2}$ state reported in Table 2. ^c Accessing the lowest spin-orbit cationic state. ^d This is the experimental spin-orbit splitting for the ... np^5 ground electronic state configuration.³⁹

constants in Tables 1 and 2 should be the same for these two states. Indeed, they are essentially identical for RG = He–Ar for Si⁺–RG, and for RG = He and Ne for Ge⁺–RG, but significant, increasing deviations, occur as the atomic number of RG increases. We attribute this to “contamination” of the SA-CASSCF wavefunction employed for the spin-orbit calculations by contributions that affect the values from the diagonalized spin-orbit matrix, and consequently the spin-orbit curves. This behaviour was also observed for the C⁺–RG complexes.³⁷

3.3 Comparison to ... $np^1(n+1)s^1$ neutral excited states

For C, Si or Ge, if one of the np electrons of the ground electronic state is excited to a high-lying, Rydberg s orbital, this will lead to a ... p^1 ionic core. For the complex, one might expect to produce a state whose spectroscopic parameters would be close to those of the ion itself, *i.e.* to those of C⁺–Ar, for example. However, for low values of n , as is the case for the 3s Rydberg states of NO interacting with RG,^{67–69} there is expected to be a competition between the Rydberg electron and the RG atom, for the region close to the cationic core. This is expected to lead to a weakening of the cation–RG interaction in a Rydberg state of a complex over that of the cation itself. Such a picture was also seen for the related 6p \leftarrow 6s excitation in Au–RG complexes, where the binding energy of the excited $^2\Pi_{3/2}$ state was calculated to be less strongly bound than was the corresponding cation.⁶⁶

Although the electronic spectroscopy of C–Ar has been studied experimentally, spectra arose there from states arising from the $2s^12p^3 \leftarrow 2s^22p^2$ atomic transition.⁷⁰ States arising from the $2s^22p^13s^1 \leftarrow 2s^22p^2$ transition were deduced to be predissociated, and these states have been studied theoretically, including spin-orbit interactions.⁷¹ From that work, the vibrational wavenumber of the upper state, designated B³ Π

therein, can be derived from the given vibrational energy levels as 413 cm⁻¹, which is slightly less than the value for C⁺–Ar that we calculated previously³⁷ – and is in line with the expectations outlined in the previous paragraph. (In a similar way, a calculated value for the B³ Π state of $\omega_e x_e = 5.4$ cm⁻¹ can be obtained, close to the value of 4.2 cm⁻¹ reported for the $^2\Pi$ state of C⁺–Ar in our previous work.³⁷) Also, the D_0 value was derived as 4895 cm⁻¹, which is significantly less than the calculated values for C⁺–Ar ($^2\Pi$) of very close to 8000 cm⁻¹,³⁷ consistent with shielding of the C⁺ core by the 3s electron. In ref. 71, the “heavy atom” effect was invoked, whereby the carbon “borrows” spin-orbit coupling from the Ar atom, analogous to the discussion given earlier herein for the present cases, and in previous work for C⁺–RG.³⁷

Looking now at the ... $3s^23p^14s^1 \leftarrow \dots 3s^23p^2$ transition in Si–Ar, this has been studied experimentally by Dedonder-Lardeux *et al.*,⁷² who derive a value for ω_e of 200.5 cm⁻¹ for the $^3\Pi_1$ state. This can be compared to the interaction of Ar with Si⁺... $3s^23p^1\ ^2P$, with the value for the $^3\Pi_1$ state being higher than the calculated value here for the $^2\Pi_{3/2}$ state of the cation (Table 1), of 168.1 cm⁻¹. The dissociation energy of ~ 2010 cm⁻¹ in ref. 72 was refined to a value of ~ 1890 cm⁻¹ by Tao *et al.*⁷³ and this latter value is significantly below that of the corresponding value in Si⁺–Ar (see Table 1 and ref. 38), which would be consistent with the Ar atom being shielded from the Si⁺ by the 4s electron in the $^3\Pi$ state. The authors of ref. 72 discussed the nature of the observed $^3\Pi$ excited state, and concluded that it was not wholly Rydberg-like in character, and hypothesised interactions with higher electronic states. Given the differing behaviour of the dissociation energy and the vibrational wavenumber, this would be consistent with a potential energy curve that was changing its character with internuclear separation; the role of interactions of the



penetrating 4s electron with the ionic core could also then be dependent on this separation.

Also, spin-orbit transitions of the corresponding state in Ge-Ar have been studied by Tao and Dagdigian.⁷⁴ From detailed analyses of the spectra of different isotopologues, they were able to deduce absolute vibrational numbering, and hence values for ω_e and $\omega_e x_e$, which differed for different spin-orbit states. Vibrational constants were derived for three spin-orbit levels, with two ω_e values (for the $\Omega = 0^-$ and 0^+ states) being in the range 164–168 cm^{-1} , while one (for the $\Omega = 2$ state) was $\sim 194 \text{ cm}^{-1}$. These are all significantly higher than the calculated values for the $^2\Pi$ state of Ge^+-Ar , calculated here, and also the $\omega_e x_e$ values were also quite different to the present ones – see Table 2. Also, dissociation energies were estimated, with upper bounds for D_0 values for three spin-orbit levels, $\Omega = 0^-$, 0^+ and 2 being 1012 cm^{-1} , 1322 cm^{-1} and 1714 cm^{-1} , respectively; these are all significantly less than the values calculated here for Ge^+-Ar , and this is also true for the corresponding “Morse” values of $D_e (= \omega_e^2/4\omega_e x_e)$ of 1130 cm^{-1} , 1404 cm^{-1} and 1855 cm^{-1} , that can be obtained from the ω_e and $\omega_e x_e$ values reported therein. Thus, as with Si-Ar in the previous paragraph, the experimental dissociation energies being lower than that of the cation is consistent with that expected for a Rydberg state, while the higher ω_e values are not. Again, it is plausible that interactions with other higher-lying states are perturbing the potentials of the $^3\Pi_\Omega$ states, and this is supported by the suggestion⁷⁴ that barriers in the potential energy curves are present in the $^3\Pi_\Omega$ potentials. In addition, the penetrating 5s electron can interact with the ion core electrons and Ar atom, so that the Ge-Ar states are far from Rydberg-like in character.

In summary, although the calculated values for the $\dots 2s^1 2p^1 3s^1 \ ^3\Pi$ state of C-Ar are in line with expectations if it were a Rydberg state, this is not wholly the case for the

corresponding states of Si-Ar and Ge-Ar, where the dissociation energies and the ω_e values show discrepant behaviour with expectations. It can be seen from the Birge-Sponer plots in Fig. 4 and 5 that the vibrational spacings of the cation do not follow that expected for a simple Morse potential, but also it is possible that spin-orbit interactions, together with involvement of higher electronic states, are also the source of these anomalies. Spin-orbit interactions between states that arose from the $6p \leftarrow 6s$ excitation in Au-RG complexes, led to complications to the derived curves, such as a “shelf” in the $^2\Pi_{1/2}$ state of Au-Ar,⁷⁵ and the lack of a minimum in the $^2\Pi_{1/2}$ state of Au-Ne.⁶⁶

It is also interesting to see that the spectroscopy of the states that arise from the $\dots np^1(n+1)s^1$ configuration is so different, with those of C-Ar being predissociative, only the $^3\Pi_1$ state being seen for Si-Ar, while three $^3\Pi_\Omega$ levels were observed for Ge-Ar. These differences likely arise from a combination of the differing spin-orbit interactions, and also the different jet expansion conditions that led to different lower Ω -state populations in the experiments, as suggested in that work.

3.4 Ion transport

In Fig. 6 and 7 we show the zero-field mobilities for each of $^{28}\text{Si}^+$ and $^{74}\text{Ge}^+$ moving through a bath of each RG, as a function of the bath temperature. In Fig. 8 and 9, we show the calculated ion mobilities of each of $^{28}\text{Si}^+$ and $^{74}\text{Ge}^+$ moving through a bath of each RG at 300 K, as a function of E/n_0 . (Other ion transport data, at a range of different temperatures have been deposited in an online database.⁶⁰)

We first make some general comments regarding mobility. Not only does the gas temperature affect the average energy of a collision between an ion and a neutral, so does E/n_0 . The primary difference is that the average collision energy is directly

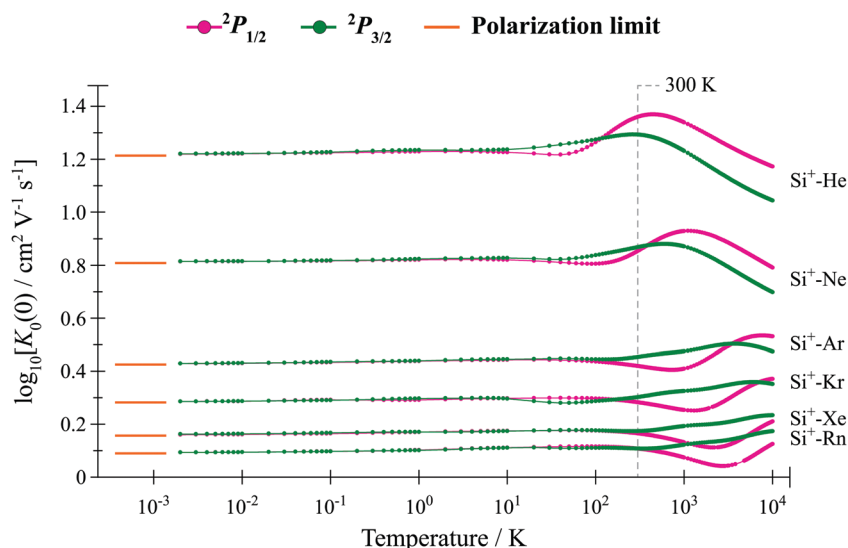


Fig. 6 Calculated zero-field mobilities versus T for the $^2P_{1/2}$ and $^2P_{3/2}$ states of $^{28}\text{Si}^+-\text{RG}$ presented as a log–log plot. The polarization limit is given in each case at the left-hand side of the plot. The RG bath was taken as a mixture of isotopes with their natural abundances; although a single isotope of Si^+ was employed here, in fact the mobilities will be quite similar for all naturally-occurring isotopes, with the full set of data included in an online database.⁶⁰ (Note that each RG will condense at the lowest T values reported herein.)



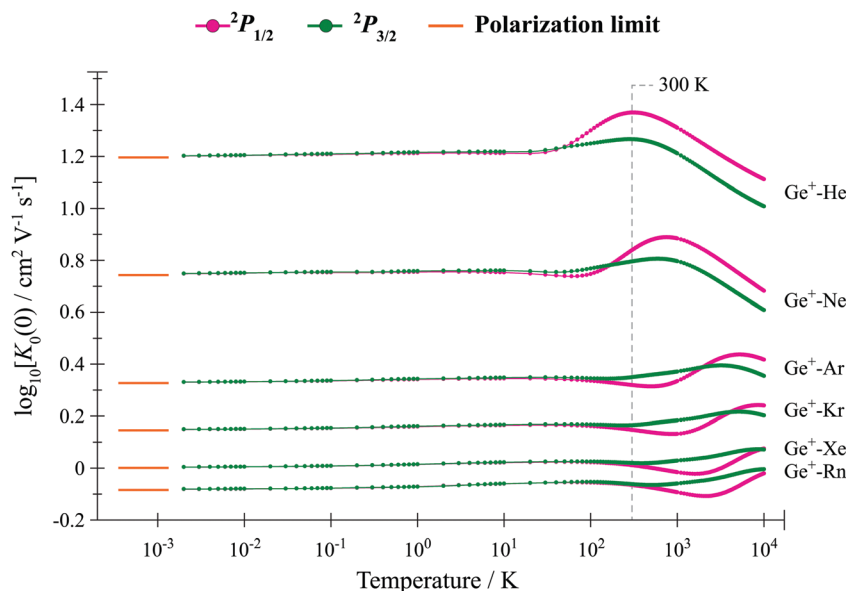


Fig. 7 Calculated zero-field mobilities versus T for the $^2P_{1/2}$ and $^2P_{3/2}$ states of $^{74}\text{Ge}^+$ –RG presented as a log–log plot. The polarization limit is given in each case at the left-hand side of the plot. The RG bath was taken as a mixture of isotopes with their natural abundances; although a single isotope of Ge^+ was employed here, in fact the mobilities will be quite similar for all naturally-occurring isotopes, with the full set of data included in an online database.⁶⁰ (Note that each RG will condense at the lowest T values reported herein.)

proportional to T but its dependence upon E/n_0 is not analytic. Increasing E causes the ion to continually accelerate between collisions, while increasing n_0 decreases the time between collisions; the two effects are exactly balanced within the E/n_0 ratio.

Consider a special case first, where the electric field is negligible: then both the ions and neutrals are moving with thermal energy. To a good approximation, the temperature dependence of the mobility then varies as $T^{1/2}\bar{\Omega}^{(1,1)}$, where $\bar{\Omega}^{(1,1)}$ is a collision integral, which contains the effect of the ion–RG potential.⁷⁶ At very low temperatures, the interactions between the collision partners are dominated by the long-range potential, which approaches the ion/induced-dipole limit for long R , and hence varies as R^{-4} ; then $\bar{\Omega}^{(1,1)}$ varies as $T^{-1/2}$, so that overall, the mobility is expected to be largely independent of T , as is seen in Fig. 6 and 7 for the lower values of T . The zero-field mobility, $K_0(0)$, at 0 K, is called the polarization limit, K_p , and its value is given⁷⁶ by the expression $\frac{13.876}{(\alpha\mu)^{1/2}}$ in units of

$\text{cm}^2 \text{V}^{-1} \text{s}^{-1}$, where α is the polarizability of RG in \AA^3 , and μ is the reduced mass of the ion/RG system in g mol^{-1} ; its value is indicated in Fig. 6 and 7 for each system. (We highlight that it takes incredibly low gas temperatures for the mobility to be almost identical with the polarization limit.) As T starts to increase, more collisions sample the interaction potential to smaller separations. If, at these smaller separations, the potential is still close to the ion–dipole potential, the mobility is little changed. As T continues to increase, an increasing number of collisions probe smaller internuclear separations, where attractive terms of higher orders than ion/induced dipole become important, and the mobility usually increases. This continues until eventually the role of the repulsive part of the

potential will become the most important, eventually causing a reduction in the mobility along the drift tube axis. The observed mobility is thus the overall result of the combined effects of the attractive and repulsive parts of the potential that are experienced by the collisions. Interestingly, the higher-order attractive terms can often cause a mobility minimum to appear, whereby the mobility is lower than the polarization limit – see Fig. 6 and 7. These occur at lower temperatures, and are then followed by a rise in mobility towards a maximum; the mobility minima are not well understood, but are thought to arise when the collision complex is particularly stable.⁷⁶ (When it occurs, it is generally accepted that the maximum in the zero-field mobility occurs when the majority of collisions experience the interaction potential close to its minimum.) It is important to acknowledge that the repulsive part of the potential increases rapidly for smaller separations – much faster than the corresponding changes for the attractive parts of the potential. As a consequence, at even higher T , where many of the separations experienced during the collisions are even shorter, the repulsive parts of the potential dominate the collisions, leading to the mobility decreasing monotonically as T continues to increase.

At a fixed temperature, such as 300 K, the mobility value as $E/n_0 \rightarrow 0$ (see Fig. 8 and 9) is the same as the zero-field mobility (see Fig. 6 and 7) at that temperature – we have marked the position of 300 K in Fig. 6 and 7. The behaviour of K_0 as E/n_0 increases is qualitatively the same as just described for $K_0(0)$ and temperature; the quantitative difference is that the collision energy (sometime described in terms of an effective temperature) is not directly proportional to E/n_0 .

In the present situations, if a mobility experiment were to be undertaken for either Si^+ or Ge^+ moving through a bath of RG,



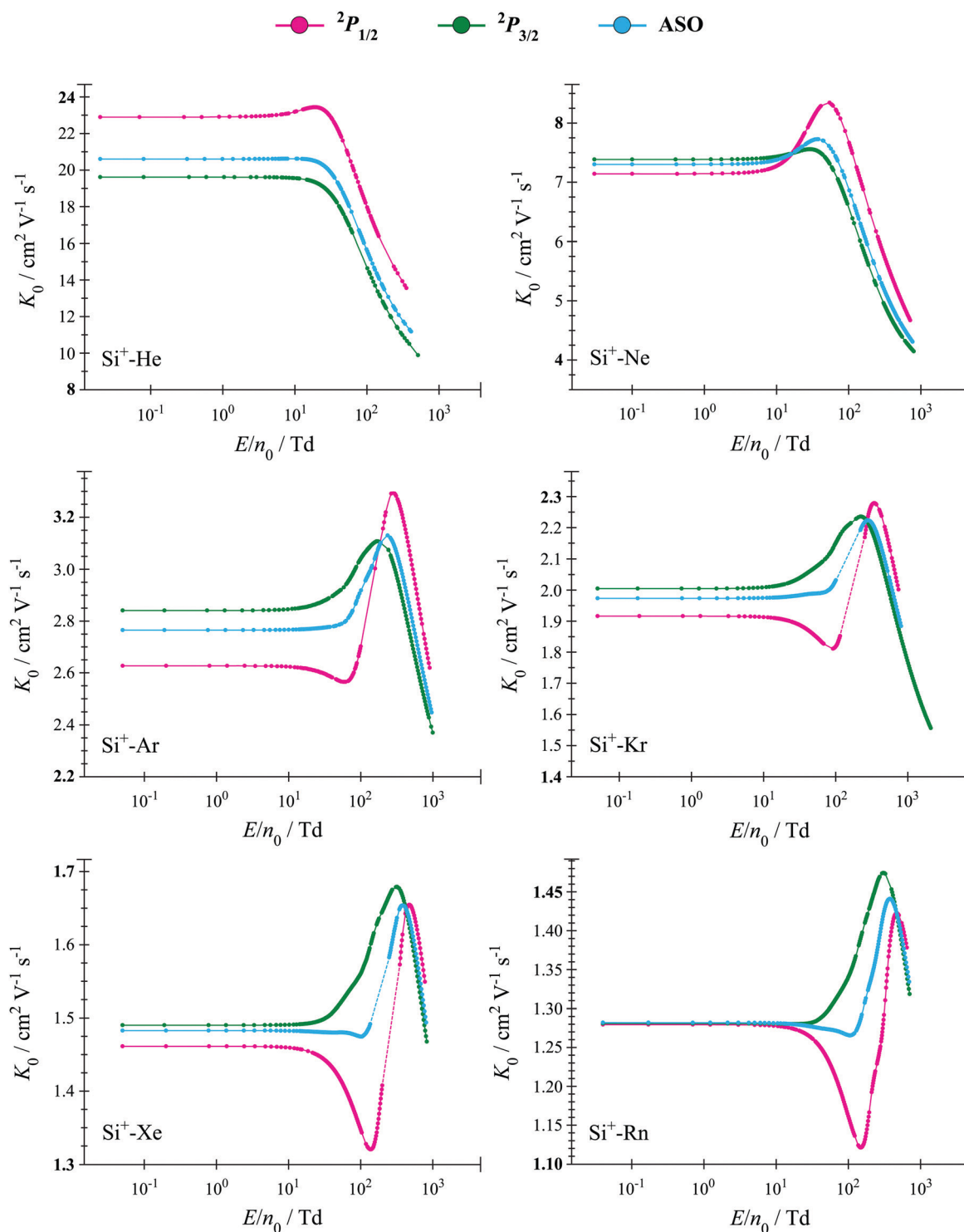


Fig. 8 Calculated reduced ion mobilities, K_0 , versus E/n_0 for $^{28}\text{Si}^+$ in a bath of RG at 300 K, presented as semi-logarithmic plots. Note that the ordinate scales are not the same for all plots. In all plots, the values for solely $^2P_{1/2}$ and solely $^2P_{3/2}$ states are given, as well as a statistical mix of the two, denoted ASO. The legend at the top of the figure applies to all plots. The RG bath was taken as a mixture of isotopes with their natural abundances; although a single isotope of Si^+ was employed here, in fact the mobilities will be quite similar for all naturally-occurring isotopes, with the full set of data included in an online database.⁶⁰ Calculated data points are shown, with the lines merely being a guide to the eye; the dashed line indicated regions where the ion transport coefficients did not converge satisfactorily. [Units on the abscissa are townsend ($1 \text{ Td} = 10^{-17} \text{ V cm}^2$).].

then we would expect the ground state cation, $^2P_{1/2}$, to be the predominant ion under thermal conditions. However, it is

possible that the excited spin-orbit level, $^2P_{3/2}$, may also be present, depending on how the ions were produced. Indeed,

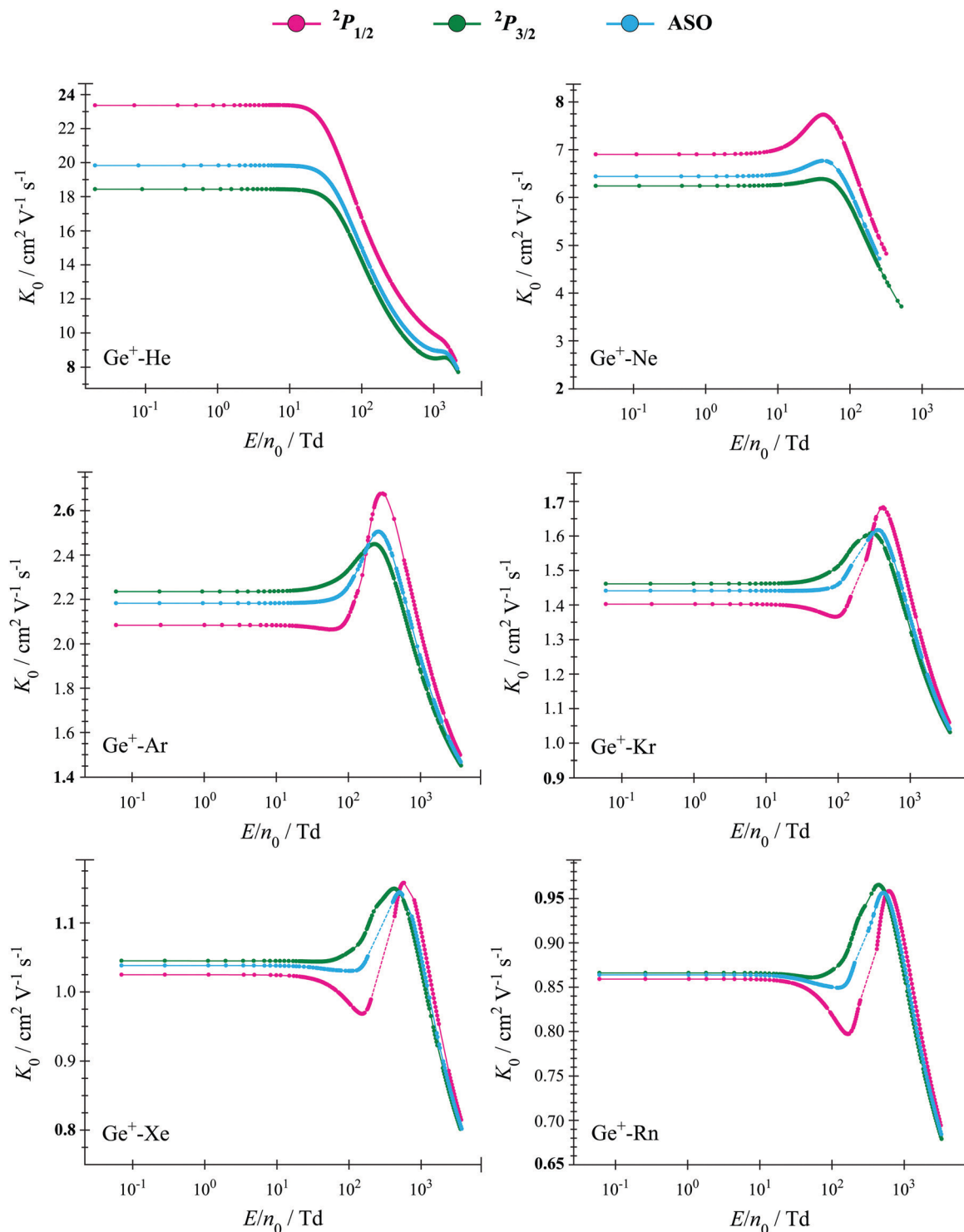


Fig. 9 Calculated reduced ion mobilities, K_0 , versus E/n_0 for $^{74}\text{Ge}^+$ in a bath of RG at 300 K, presented as semi-logarithmic plots. Note that the ordinate scales are not the same for all plots. In all plots, the values for solely $^2P_{1/2}$ and solely $^2P_{3/2}$ states are given, as well as a statistical mix of the two, denoted ASO. The legend at the top of the figure applies to all plots. The RG bath was taken as a mixture of isotopes with their natural abundances; although a single isotope of Ge^+ was employed here, in fact the mobilities will be quite similar for all naturally-occurring isotopes, with the full set of data included in an online database.⁶⁰ Calculated data points are shown, with the lines merely being a guide to the eye; the dashed line indicated regions where the ion transport coefficients did not converge satisfactorily. [Units on the abscissa are townsend (1 Td = 10^{-17} V cm²).]

there was evidence³⁶ that both spin-orbit states were present in ion mobility experiments^{77–82} involving C^+ in He, while

calculations³⁷ indicated that those for C^+ in Ar^{83} seemed to have a predominance of $^2P_{1/2}$. In addition, electronically excited C^+



has also been observed in ion mobility experiments.^{36,80} To investigate the possible differences between the mobility behaviour of these two spin-orbit states as a function of RG, we show the calculated mobilities for both spin-orbit states of Si⁺ in all RG (Fig. 8) and Ge⁺ in all RG (Fig. 9); in addition, we show the mobility for what would be an equal mixture of the two spin-orbit states, denoted ASO. In Fig. 8, we have included the results for Si⁺ in He, Ne and Ar, reported in ref. 38 for comparison; in that work we also reported comparison of calculated mobilities with previous calculated and experimental values,^{84,85} concluding that there was not enough experimental detail to be sure of a fair comparison, although the comparison was suggestive of a mixture of spin-orbit states in the experiments. The mobility curves in Fig. 8 and 9 each show mobility maxima and that a mobility minimum develops for the heavier RG, where the potentials are much deeper, owing to the stronger attractive terms in the interaction. Another interesting observation is that at low E/n_0 , the mobilities of the two spin-orbit states are not in the same order for all RG, although the ASO curve is always closer to that of the $^2P_{3/2}$ state. This differing mobility would mean that for a particular system, ions in one or the other spin-orbit states would arrive first at the detector, and so provide a means for state selection.

To understand the latter point, we comment that for the cations under consideration here, if we initially ignore spin-orbit effects, then collisions can occur that sample the $^2\Sigma^+$ curve or the $^2\Pi$ curve, with the latter having the larger interaction energy. Thus, mobilities of ions in the $^2\Pi$ state would be expected to be different to those in the $^2\Sigma^+$ state. Things are more complicated here as spin-orbit coupling mixes these states: the $^2\Pi_{1/2}$ state contains mostly $^2\Pi$ character, but with some $^2\Sigma^+$, while the $^2\Sigma_{1/2}^+$ state is largely of $^2\Sigma^+$ character, with some $^2\Pi$; the $^2\Pi_{3/2}$ state is expected to be purely $^2\Pi$ in character, with some caveats, as discussed above. When we then consider the atomic cations, we recall that the $^2P_{3/2}$ state evolves along two potential energy curves, $^2\Pi_{3/2}$ and $^2\Sigma_{1/2}^+$, while the $^2P_{1/2}$ state evolves along the single $^2\Pi_{1/2}$ curve – see Fig. 1 and 2. For the $^2P_{3/2}$ state, therefore, it is the combined effects of the $^2\Sigma_{1/2}^+$ and $^2\Pi_{3/2}$ states on the collision cross-sections that will determine its mobility, while it is solely that of the $^2\Pi_{1/2}$ state for $^2P_{1/2}$; thus for both atomic spin-orbit states, there are (different) contributions from both non-spin-orbit diatomic states. As the atomic number of the rare gas gets larger, the $^2\Pi$ potential gets deeper (Fig. 1 and 2), and the repulsive part of the $^2\Sigma^+$ potential is expected to start to rise more steeply at progressively larger values of internuclear separation (thus, the degree of mixing of the $^2\Sigma^+$ and $^2\Pi$ states in the spin-orbit states will vary with R); these two effects will affect the mobility in opposite directions, making it difficult to predict the final ordering of the $^2P_{3/2}$ and $^2P_{1/2}$ mobilities. The overall balance of these effects on the two spin-orbit states can be seen to be quite subtle, since at low E/n_0 : for C⁺/RG, the $^2P_{3/2}$ mobility is the higher for He–Kr, then switches for Xe;^{36,37} for Si⁺/RG, the $^2P_{3/2}$ mobility is the lower for He, then switches for Ne–Rn; while, for Ge⁺/RG, the $^2P_{3/2}$ mobility is the lower for

He and Ne, then switches for Ar–Rn. For the zero-field mobilities as a function of temperature (Fig. 6 and 7), again it is evident that the ordering of the $K_0(0)$ values for the two spin-orbit levels is not consistent across the RG series, and is also rationalized by the subtle effects mentioned above.

Finally, we did not consider C⁺ interacting with Rn in our earlier work.^{36,37} We have now undertaken some calculations, but this system is more complicated, since the ionization energy of Rn is lower than that of C⁺; as such the lowest electronic state will arise from the C(3P_0) + Rn($^2P_{3/2}$) asymptote. If, however, a mobility experiment for C⁺ passing through Rn were undertaken, then the interactions would be dictated by C⁺–Rn curves. Hence, we would expect some charge transfer to occur during such an experiment, and so the C⁺ signal to deplete, and some Rn⁺ ions formed. Given the esoteric nature of the [C/Rn]⁺ system, we refrain from reporting and discussing our calculations in full, but note that the mobility data for C⁺ in Rn have been calculated using the same methods reported herein and in ref. 37, and these are available in an online database.⁶⁰

4. Concluding remarks

Here, we have presented high-level calculated potentials for Si⁺–RG (RG = Kr–Rn) and Ge⁺–RG (RG = He–Rn). These have been used to obtain spectroscopic constants, which, based on experience with a number of other systems, are expected to be very reliable. We have discussed the trends in the main constants as RG varies, finding that there is a balance between the increasing size and polarizability of the RG atom, as far as R_e is concerned, while the dissociation energy and force constants increase monotonically with the atomic number of RG; as usual, the harmonic vibrational wavenumber has both mass and force constant variations, which, again, act in opposite directions. We also suggested that the Si⁺–He and Ge⁺–He potentials may be useful in investigations of ion cooling in interstellar chemistry.

We have commented on the nature of the interactions in terms of the calculated charges on the different atoms, and the calculated spin-orbit splitting in the complex compared to that in the isolated atoms. We conclude that for the RG atoms with a higher atomic number, the role of charge-transfer with the RG atom is likely to be becoming increasingly important – this has the most notable effect for C⁺–RG, less so for Si⁺–RG, much smaller in the case of Ge⁺–RG. This trend is likely due to the decreasing ionization energy from C → Ge.

Interestingly, if one calculates the ionic radius of the ions C⁺, Si⁺ and Ge⁺ using the ideas presented in ref. 86, whereby 1.49 Å is subtracted from the M⁺–He R_e value, then different values are obtained for the $^2\Pi$ and $^2\Sigma^+$ states. For the former, values of 0.71 Å, 1.28 Å and 1.22 Å are obtained, while for the latter 1.48 Å, 2.37 Å and 2.43 Å, respectively. These values are different, owing to the different orientation of the unpaired p electron; furthermore, the trend for $^2\Pi$ states is not monotonically increasing, probably related to a balance of factors



discussed above when focusing on the RG atom, in relation to the trends shown in Fig. 3. These facts illustrate that it is difficult to arrive at a unique value for an ionic radius – see further commentary in ref. 86 – particularly in non-spherically-symmetric environments.

We have discussed the comparison of the spectroscopic constants of $\dots np^1(n+1)s^1$ states of C–Ar, Si–Ar and Ge–Ar with those of the corresponding cation, finding unexpected results. In line with previous suggestions, we attribute this to the penetrating nature of the $(n+1)s$ electron, which will lead to an increase in their interaction with the cationic core. This, and the differing magnitudes of the atomic spin–orbit coupling, will affect the effect of spin–orbit coupling in the complex. It would be of great interest to study related species with different RG atoms, and for ns states for larger principal quantum number.

We have also used the potentials to calculate ion transport properties, with the mobilities of the atomic cation in a bath of each RG discussed herein. We have highlighted that the behaviour of the two atomic spin–orbit states is complicated owing to the differing roles of the repulsive and attractive aspects of the underlying potentials; particularly, as these are each admixtures of the underlying $^2\Sigma^+$ and $^2\Pi$ states, which become mixed by spin–orbit coupling. Nonetheless, earlier work on C^+/RG has shown that the calculated mobility curves can be used to gain insight into the ionic state populations that may be present in an experiment. Further, this differing behaviour may then be used to separate different states. We highlight that the bulk properties of ion mobilities and other transport coefficients are exquisitely sensitive to the potential energy surfaces, and so provide a robust test of such potentials, if precise and accurate experimental data are available to which to compare.

Author contributions

TGW conceived and supervised the research and wrote the manuscript. AC performed quantum chemistry calculations and approved the final version of the manuscript. ARD performed quantum chemistry calculations, undertook analyses, commented on drafts of the manuscript and approved the final version. LAV performed the transport coefficient calculations, commented on drafts of the manuscript and approved the final version.

Conflicts of interest

The authors declare that they have no competing interests.

Acknowledgements

We are grateful for access to the University of Nottingham High Performance Computing Facility. The EPSRC and the University of Nottingham are thanked for the provision of a studentship to A. R. D.

References

- 1 T. I. Kamins and D. J. Meyer, *Appl. Phys. Lett.*, 1991, **59**, 178.
- 2 S. Nunomura and M. Kondow, *Appl. Phys. Lett.*, 2008, **93**, 231502.
- 3 S. Yamada, S. Oguri, A. Morimoto, T. Shimizu, T. Minamikawa and Y. Yonezawa, *Jpn. J. Appl. Phys.*, 2000, **39**, 278.
- 4 G. Dushaq, M. Rasras and A. Nayfeh, *Thin Solid Films*, 2017, **636**, 585.
- 5 J. M. C. Plane, J. C. Gómez-Martin, W. Feng and D. Janches, *J. Geophys. Res.: Atmos.*, 2016, **121**, 3718.
- 6 R. J. Plowright, T. J. McDonnell, T. G. Wright and J. M. C. Plane, *J. Phys. Chem. A*, 2009, **113**, 9354.
- 7 C. L. Whalley, J. C. Gomez Martin, T. G. Wright and J. M. C. Plane, *Phys. Chem. Chem. Phys.*, 2011, **13**, 6352.
- 8 R. J. Plowright, T. G. Wright and J. M. C. Plane, *J. Phys. Chem. A*, 2008, **112**, 6550.
- 9 S. Broadley, T. Vondrak, T. G. Wright and J. M. C. Plane, *Phys. Chem. Chem. Phys.*, 2008, **10**, 5287.
- 10 S. E. Daire, J. M. C. Plane, S. D. Gamblin, P. Soldán, E. P. F. Lee and T. G. Wright, *J. Atmosph. Solar-Terrestrial Phys*, 2002, **64**, 863.
- 11 J. M. C. Plane, R. J. Plowright and T. G. Wright, *J. Phys. Chem. A*, 2006, **110**, 3093.
- 12 T. Vondrák, K. R. I. Woodcock and J. M. C. Plane, *Phys. Chem. Chem. Phys.*, 2006, **8**, 1812.
- 13 E. Kopp, F. Balsiger and E. Murad, *Geophys. Res. Lett.*, 1995, **22**, 3473.
- 14 E. E. Ferguson, D. W. Fahey, F. C. Fehsenfeld and D. L. Albritton, *Planet. Space Sci.*, 1981, **29**, 307.
- 15 P. Boschler, *J. Geophys. Res. Space Phys.*, 1989, **94**, 2365.
- 16 S. Wlodek, D. K. Bohme and E. Herbst, *Mon. Not. R. Astron. Soc.*, 1990, **242**, 674.
- 17 E. Herbst, T. J. Millar, S. Wlodek and D. K. Bohme, *Astron. Astrophys.*, 1989, **222**, 205.
- 18 S. Fornarini, *Ion–Molecule Reactions of Silicon Cations. Patai's Chemistry of Functional Groups*, Wiley Online, 1992, DOI: 10.1002/9780470682531.pat0252.
- 19 J. H. Horton and J. M. Goodings, *Can. J. Chem.*, 1992, **70**, 1069.
- 20 S. Morozova, M. Alikina, A. Vinogradov and M. Pagliaro, *Front. Chem.*, 2020, **8**, 191.
- 21 J. T. Wasson, *Science*, 1966, **153**, 976.
- 22 L. M. Hobbs, D. E. Welty, D. C. Morton, L. Spitzer and D. G. Tork, *Astrophys. J.*, 1993, **411**, 750.
- 23 S. I. B. Cartledge, J. T. Lauroesch, D. M. Meyer and U. J. Sofia, *Astrophys. J.*, 2006, **641**, 327.
- 24 E. B. Jenkins, *Astrophys. J.*, 2009, **700**, 1299.
- 25 S. W. Harrison, G. A. Henderson, L. J. Massa and P. Solomon, *Astrophys. J.*, 1974, **189**, 605.
- 26 N. Toshima, *J. Phys. Soc. Jpn.*, 1975, **38**, 1464.
- 27 J. M. Curtis and L.-S. Rong, *Rap. Comm. Mass Spectrom.*, 1991, **5**, 62.
- 28 J. C. Gómez-Martín, M. A. Blitz and J. M. C. Plane, *Phys. Chem. Chem. Phys.*, 2009, **11**, 671.
- 29 J. C. Gómez-Martín, M. A. Blitz and J. M. C. Plane, *Phys. Chem. Chem. Phys.*, 2009, **11**, 10945.



- 30 J. C. Gómez-Martín and J. M. C. Plane, *Phys. Chem. Chem. Phys.*, 2011, **13**, 3764.
- 31 L. A. Viehland, A. Lutfullaeva, J. Dashdorj and R. Johnsen, *Int. J. Ion Mob. Spectrom.*, 2017, **20**, 95.
- 32 E. Carbone, W. Graef, G. Hagelaar, D. Boer, M. M. Hopkins, J. C. Stephens, B. T. Yee, S. Pancheshnyi, J. van Dijk and L. Pitchford, *Atoms*, 2021, **9**, 16.
- 33 S. Pan, G. Jana, G. Merino and P. K. Chattaraj, *ChemistryOpen*, 2019, **8**, 173.
- 34 C. J. Evans, T. G. Wright and A. M. Gardner, *J. Phys. Chem. A*, 2010, **114**, 4446–4454.
- 35 W. D. Tuttle, J. P. Harris, Y. Zheng, W. H. Breckenridge and T. G. Wright, *J. Phys. Chem. A*, 2018, **122**, 7679.
- 36 W. D. Tuttle, R. L. Thorington, L. A. Viehland and T. G. Wright, *Molec. Phys.*, 2015, **113**, 3767.
- 37 W. D. Tuttle, R. L. Thorington, L. A. Viehland, W. H. Breckenridge and T. G. Wright, *Phil. Trans. Roy. Soc. Lond.*, 2018, **376**, 20170156.
- 38 W. D. Tuttle, R. L. Thorington, L. A. Viehland and T. G. Wright, *Mol. Phys.*, 2017, **115**, 437.
- 39 *Spectra Database (ver. 5.9)*, <https://physics.nist.gov/asd> [accessed: 2021, November 29]. National Institute of Standards and Technology, Gaithersburg, MD, DOI: 10.18434/T4W30F.
- 40 H.-J. Werner, P. J. Knowles, G. Knizia, F. R. Manby, M. Schütz, P. Celani, T. Korona, R. Lindh, A. Mitrushenkov, G. Rauhut, K. R. Shamasundar, T. B. Adler, R. D. Amos, A. Bernhardsson, A. Berning, D. L. Cooper, M. J. O. Deegan, A. J. Dobbyn, F. Eckert, E. Goll, C. Hampel, A. Hesselmann, G. Hetzer, T. Hrenar, G. Jansen, C. Köppl, Y. Liu, A. W. Lloyd, R. A. Mata, A. J. May, S. J. McNicholas, W. Meyer, M. E. Mura, A. Nicklaß, D. P. O'Neill, P. Palmieri, D. Peng, K. Pflüger, R. Pitzer, M. Reiher, T. Shiozaki, H. Stoll, A. J. Stone, R. Tarroni, T. Thorsteinsson and M. Wang, *MOLPRO is a package of ab initio programs*.
- 41 H. J. Werner, P. J. Knowles, G. Knizia, F. R. Manby and M. Schütz, *WIREs Comput. Mol. Sci.*, 2012, **2**, 242, DOI: 10.1002/wcms.82.
- 42 D. E. Woon and T. H. Dunning, *J. Chem. Phys.*, 1994, **100**, 2975.
- 43 K. A. Peterson and T. H. Dunning, Jr, *J. Chem. Phys.*, 2002, **117**, 10548.
- 44 B. Metz, H. Stoll and M. Dolg, *J. Chem. Phys.*, 2000, **113**, 2563.
- 45 K. A. Peterson, D. Figgen, E. Goll, H. Stoll and M. Dolg, *J. Chem. Phys.*, 2003, **119**, 11113.
- 46 A. Berning, M. Schweizer, H. J. Werner, P. J. Knowles and P. Palmieri, *Mol. Phys.*, 2000, **98**, 1823.
- 47 A. Halkier, T. Helgaker, P. Jørgensen, W. Klopper, H. Koch, J. Olsen and A. K. Wilson, *Chem. Phys. Lett.*, 1998, **286**, 243.
- 48 A. Halkier, T. Helgaker, P. Jørgensen, W. Klopper, H. Koch and J. Olsen, *Chem. Phys. Lett.*, 1999, **302**, 437.
- 49 T. J. Lee and P. R. Taylor, *Int. J. Quant. Chem.*, 1989, **S23**, 199.
- 50 E. D. Glendening, A. E. Reed, J. E. Carpenter and F. Weinhold, *NBO Version 3.1*.
- 51 M. J. Frisch, G. W. Trucks, H. B. Schlegel, G. E. Scuseria, M. A. Robb, J. R. Cheeseman, G. Scalmani, V. Barone, G. A. Petersson, H. Nakatsuji, X. Li, M. Caricato, A. V. Marenich, J. Bloino, B. G. Janesko, R. Gomperts, B. Mennucci, H. P. Hratchian, J. V. Ortiz, A. F. Izmaylov, J. L. Sonnenberg, D. Williams-Young, F. Ding, F. Lipparini, F. Egidi, J. Goings, B. Peng, A. Petrone, T. Henderson, D. Ranasinghe, V. G. Zakrzewski, J. Gao, N. Rega, G. Zheng, W. Liang, M. Hada, M. Ehara, K. Toyota, R. Fukuda, J. Hasegawa, M. Ishida, T. Nakajima, Y. Honda, O. Kitao, H. Nakai, T. Vreven, K. Throssell, J. A. Montgomery, Jr., J. E. Peralta, F. Ogliaro, M. J. Bearpark, J. J. Heyd, E. N. Brothers, K. N. Kudin, V. N. Staroverov, T. A. Keith, R. Kobayashi, J. Normand, K. Raghavachari, A. P. Rendell, J. C. Burant, S. S. Iyengar, J. Tomasi, M. Cossi, J. M. Millam, M. Klene, C. Adamo, R. Cammi, J. W. Ochterski, R. L. Martin, K. Morokuma, O. Farkas, J. B. Foresman and D. J. Fox, *Gaussian 16, Revision A.03*, Gaussian, Inc., Wallingford, CT, 2016.
- 52 T. A. Keith, *AIMall*, T. K. Gristmill Software, Overland Park, KS, 2011, see aim.tkgristmill.com.
- 53 R. J. Le Roy, *Level 8.0: A Computer Program for Solving the Radial Schrödinger Equation for Bound and Quasibound Levels*, University of Waterloo Chemical Physics Research Report CP-663, 2007.
- 54 L. A. Viehland and Y. Chang, *Comput. Phys. Commun.*, 2010, **181**, 1687.
- 55 L. A. Viehland, *Chem. Phys.*, 1982, **70**, 149.
- 56 L. A. Viehland, *Chem. Phys.*, 1984, **85**, 291.
- 57 L. A. Viehland, *Comput. Phys. Commun.*, 2001, **142**, 7.
- 58 D. M. Danailov, L. A. Viehland, R. Johnsen, T. G. Wright and A. S. Dickinson, *J. Chem. Phys.*, 2008, **128**, 134302.
- 59 L. A. Viehland, *Int. J. Ion Mobil. Spec.*, 2012, **15**, 21.
- 60 https://fr.lxcat.net/data/set_type.php.
- 61 D. Bellert and W. H. Breckenridge, *Chem. Rev.*, 2002, **5**, 1595.
- 62 R. J. LeRoy and R. B. Bernstein, *Chem. Phys. Lett.*, 1970, **5**, 42.
- 63 R. J. LeRoy and R. B. Bernstein, *J. Molec. Spectrosc.*, 1971, **37**, 109.
- 64 R. J. LeRoy and R. B. Bernstein, *J. Chem. Phys.*, 1970, **52**, 3869.
- 65 See, for example, D. Cremer and E. Kraka, *Angew. Chem., Int. Ed. Engl.*, 1984, **23**, 627.
- 66 R. J. Plowright, A. M. Gardner, C. D. Withers, T. G. Wright, M. D. Morse and W. H. Breckenridge, *J. Phys. Chem. A*, 2010, **114**, 3103.
- 67 S. D. Gamblin, S. E. Daire, J. Lozeille and T. G. Wright, *Chem. Phys. Lett.*, 2000, **325**, 232.
- 68 J. Lozeille, S. E. Daire, S. D. Gamblin, T. G. Wright and D. M. Smith, *J. Chem. Phys.*, 2000, **113**, 7224.
- 69 V. L. Ayles, R. J. Plowright, M. J. Watkins, T. G. Wright, J. Klos, M. H. Alexander, P. Pajón-Suarez, J. Rubayo-Soneira and R. Hernández-Lamonedá, *Chem. Phys. Lett.*, 2007, **441**, 181.
- 70 J. Lei and P. J. Dagdigian, *J. Chem. Phys.*, 2000, **113**, 602.
- 71 K. Sohlberg and D. R. Yarkony, *J. Chem. Phys.*, 1999, **111**, 3070.



- 72 C. Dedonder-Lardeux, C. Jouvét, M. Richard-Viard and D. Solgadi, *J. Chem. Phys.*, 1990, **92**, 2828.
- 73 C. Tao, A. Teslja, P. J. Dagdigian, S. Atahan and M. H. Alexander, *J. Chem. Phys.*, 2002, **116**, 9239.
- 74 C. Tao and P. J. Dagdigian, *J. Chem. Phys.*, 2002, **118**, 1242.
- 75 T. G. Wright, M. J. Watkins, R. J. Plowright and W. H. Breckenridge, *Chem. Phys. Lett.*, 2008, **459**, 70.
- 76 E. W. McDaniel and E. A. Mason, *The Mobility and Diffusion of Ions in Gases*, Wiley, New York, 1973.
- 77 I. Dotan, F. C. Fehsenfeld and D. L. Albritton, *J. Chem. Phys.*, 1979, **71**, 4762.
- 78 R. Thomas, J. Barassin and A. Barassin, *Int. J. Mass Spectrom. Ion Phys.*, 1979, **31**, 227.
- 79 N. Peska, Dissertation, Leopold-Franzens-Universität, 1981.
- 80 N. D. Twiddy, A. Mohebati and M. Tichy, *Int. J. Mass Spectrom. Ion Proc.*, 1986, **74**, 251.
- 81 S. T. Grice, P. W. Harland, R. G. A. R. Maclagan and R. W. Simpson, *Int. J. Mass Spectrom. Ion Proc.*, 1989, **87**, 181.
- 82 S. Matoba, H. Tanuma and K. Ohtsuki, *J. Phys. B: At., Mol. Opt. Phys.*, 2008, **41**, 145205.
- 83 E. Basurto and J. de Urquijo, *J. Appl. Phys.*, 2002, **91**, 36.
- 84 D. W. Fahey, F. C. Fehsenfeld, E. E. Ferguson and L. A. Viehland, *J. Chem. Phys.*, 1981, **75**, 669.
- 85 S. T. Grice, P. W. Harland, R. G. A. R. Maclagan and A. E. Thompson, *J. Chem. Soc., Faraday Trans.*, 1995, **91**, 4355.
- 86 T. G. Wright and W. H. Breckenridge, *J. Phys. Chem. A*, 2010, **114**, 3182.

